CHEMISTRY

# Enabling reversible redox reactions in electrochemical cells using protected LiAl intermetallics as lithium metal anodes

Mun Sek Kim[1,2], Deepika[3], Seung Hun Lee[1], Min-Seop Kim[1,4], Ji-Hyun Ryu[1,4], Kwang-Ryeol Lee[3], Lynden A. Archer[5]*, Won Il Cho[1]*

Copyright © 2019 The Authors, some rights reserved; exclusive licensee American Association for the Advancement of Science. No claim to original U.S. Government Works. Distributed under a Creative Commons Attribution NonCommercial License 4.0 (CC BY-NC).

**Rechargeable electrochemical cells with metallic anodes are of increasing scientific and technological interest. The complex composition, poorly defined morphology, heterogeneous chemistry, and unpredictable mechanics of interphases formed spontaneously on the anodes are often examined but rarely controlled. Here, we couple computational studies with experimental analysis of well-defined LiAl electrodes in realistic electrochemical environments to design anodes and interphases of known composition. We compare phase behavior, Li binding energies, and activation energy barriers for adatom transport and study their effects on the electrochemical reversibility of battery cells. As an illustration of potential practical benefits of our findings, we create cells in which LiAl anodes protected by Langmuir-Blodgett $MoS_2$ interphases are paired with 4.1 mAh $cm^{-2}$ $LiNi_{0.8}Co_{0.1}Mn_{0.1}O_2$ cathodes. These studies reveal that small- and larger-format (196 mAh, 294 Wh $kg^{-1}$, and 513 Wh $liter^{-1}$) cells based on protected LiAl anodes exhibit high reversibility and support stable Li migration during recharge of the cells.**

## INTRODUCTION

The need for advanced battery technology that uses electrochemically active metallic anodes to achieve more energy-dense storage is now well known and widely discussed in the literature (*1*, *2*). The primary drivers of this need (smaller and more powerful portable devices; electrified transportations with greater range, improved safety features, and efficient yet faster charging; and fully autonomous unmanned vehicles for terrestrial and aerial applications) are also well known. It is known, for example, that replacing the graphite-based anode used for commercial lithium-ion batteries (LiBs) with a stable Li metal (LiM) anode and pairing the LiM anode with state-of-the-art lithiated cathodes, such as high-nickel lithium-nickel-cobalt-manganese oxide (NCM) and lithium-nickel-cobalt-aluminum oxide (NCA), could lead to advanced secondary battery designs that enhance energy density in comparison to state-of-the-art LiBs (*1*–*3*). Furthermore, the compatibility of the LiM anode with cathodes that are either unlithiated, such as $S_8$ and $O_2$, or lithiated, such as NCM and NCA, provides additional flexibility in battery designs (*4*). Beyond their relevance for driving consumer adoption of low–carbon footprint electrified storage solutions to power human mobility, stable electrochemical cell designs in which the LiM anodes are paired with any of these cathode chemistries would also require advanced electrolyte design and engineering (*5*–*8*).

It is understood that control of the compositions, physical properties, ion transport characteristics, and spatiotemporal evolution of the solid-electrolyte interphases (SEIs) formed spontaneously on the LiM anode in contact with any electrolyte (liquid, quasi-liquid, or solid) is a critical requirement for making progress (*9*). Achieving such control in tandem with approaches to address other challenges, including (i) designing self-limiting cathode-electrolyte interphases (*2*, *10*); (ii) creating electrolyte systems with long-term chemical and electrochemical stability at the electrodes (*6*, *11*–*13*); (iii) development of electrochemical cells with close to balanced anode-to-cathode capacities such as n/p ratios close to unity (*11*); and (iv) achieving stability at reasonable cycling C rates (*14*), voltage windows (*10*), temperatures (*15*), and pressures (*16*), has emerged as a grand challenge–scale problem in the field. This challenge is complicated further by unavoidable couplings of the parameters that control each of these features.

A substantial body of work has emerged in recent years that address physicochemical processes that stabilize the anode/electrolyte interface to suppress inhomogeneous Li electrodeposition/dissolution. Several effective approaches have been proposed to achieve efficient Li transport through the interphases formed on LiM anodes in aprotic liquid electrolytes and to enable high levels of reversibility in the electrochemical reactions that occur at the anodes' interphases (*17*–*19*). Among these approaches, we single out efforts that use alloying, such as Li-B, Li-Mg, and Li-In mechanisms (*20*–*26*), and coating processes to create stable and well-defined interphases on LiM (*11*, *27*, *28*) for their ability to create full electrochemical cells in which the anode and cathode capacity ratio (n/p ratio) is beginning to approach values required for a practical success of lithium metal batteries (LiMBs).

In this study, we consider the design features of a bulk metal alloy anode and the associated interphases required to achieve high levels of reversibility and satisfactory cycling performance of batteries based on the LiM anodes (*1*, *3*). A key finding is that LiMBs that use lithium-aluminum (LiAl) anodes composed of Li and the $Li_9Al_4$ intermetallic compound and a carefully designed Langmuir-Blodgett artificial SEI (LBASEI) composed of $MoS_2$ provide a strong foundation for the progress. Our specific interest in the LiAl anode is motivated by the hypothesis that the degree of Li adatom binding in the $Li_9Al_4$ intermetallic compound and the magnitude of the activation barrier for Li surface transport are the principal physical determinants of reversibility of the LiM anode. Extending our experimental assessment of this hypothesis to include systems where the intermetallic compound is protected by a compact LBASEI composed of $MoS_2$ ($MoS_2$ LBASEI) allows us to develop LiAl anode designs suitable for practical LiMBs. In-depth analyses of Li migration at the LiAl anode and at the $MoS_2$ LBASEI using first-principles calculations

[1]Center for Energy Storage Research, Korea Institute of Science and Technology, Hwarangno 14-gil 5, Seongbuk-gu, Seoul 02792, Republic of Korea. [2]School of Chemical Engineering, Stanford University, Stanford, CA 94305, USA. [3]Center for Computational Science Research, Korea Institute of Science and Technology, Hwarangno 14-gil 5, Seongbuk-gu, Seoul 02792, Republic of Korea. [4]Department of Materials Science and Engineering, Korea University, 145 Anam-ro, Seongbuk-gu, Seoul 02841, Republic of Korea. [5]School of Chemical and Biomolecular Engineering, Cornell University, Ithaca, NY 14853-5201, USA.
*Corresponding author. Email: laa25@cornell.edu (L.A.A.); wonic@kist.re.kr (W.I.C.)

Downloaded from http://advances.sciencemag.org/ on October 31, 2019

and experiments are used to evaluate the proposed hypothesis and practical benefits of LiMBs based on $MoS_2$ LBASEI–protected LiAl anodes. A key finding is that while either high or low activation energies for Li surface diffusion can be beneficial, depending on the intrinsic heterogeneity of the anode/electrolyte interphase and specific surface characteristics of the mobile species, high binding energies of Li adatoms are always preferred to achieve a high reversibility of the LiM anode. Building upon these ideas, we create LiAl anodes with preferred compositions using a simple thermal mixing process in which Li and Al powders, 80 weight % (wt %) Li and 20 wt % Al, are combined under an inert atmosphere. By roll-pressing the formed LiAl ingot, we show that it is possible to obtain LiAl foils in thicknesses suitable for battery applications. By functionalizing these foils with commercially available $MoS_2$ particles using our previously reported Langmuir-Blodgett scooping (LBS) method (*11*, *27*, *29*, *30*), we report further that it is possible to protect LiAl anodes with a well-defined, stable interphase that facilitates electrode reversibility. Last, as a proof of the practical viability of the concept, we pair $MoS_2$ LBASEI–coated LiAl ($MoS_2$ LiAl) anodes with high-loading $LiNi_{0.8}Co_{0.1}Mn_{0.1}O_2$ (NCM811) commercial cathodes with an areal capacity of 4.1 mAh $cm^{-2}$ to construct LiMBs with high practical specific energies of 294 Wh $kg^{-1}$ and 513 Wh $liter^{-1}$. It is shown that these batteries exhibit high levels of reversibility.

## RESULTS AND DISCUSSION

### Investigation of structure, adatom binding, and transport properties of the LiAl anode

Rechargeable batteries based on LiM anodes date back at least to the 1970s and emerged before the invention of graphitic carbon anodes and Li polymer electrolytes used for present-day LiBs. Lithium batteries that use LiM as counter electrodes are also widely used in research to construct so-called half cells in which the extensive reservoir of Li in the anode provides a convenient platform to examine the reversibility of working electrodes in a range of chemistries. However, safety concerns associated with rough, mossy/dendritic deposition, dendrite-induced short-circuits, and battery thermal runaway limited early progress toward practical batteries that use the LiM anode. Suppressing dendritic Li deposition on LiM anodes (*31*), therefore, drove early efforts to use Li alloys and LiM intermetallic compounds as anodes (*32*–*37*). Rao *et al.* (*32*), for example, reported lithium metal cells in which anodes composed of electroformed LiAl alloys were paired with the $TiS_2$ cathode to create room temperature operable lithium cells. The authors observed that battery failure due to the internal electrode shorting by Li dendrites can be avoided in such cell designs. By means of postmortem analysis of the anode after extended cycling, they also reported scant evidence of dendritic Li electrodeposits. LiAl intermetallic compounds have also been reported previously as anodes for high-temperature or molten-salt batteries (*34*). Their lower corrosiveness and reduced reactivity, relative to molten Li, and the high diffusivity of Li, $10^{-6}$ $cm^2$ $s^{-1}$, achieved at 700 K, are considered as the most beneficial features in this context. Unfortunately, at ambient temperature, the low diffusion rates of Li for LiAl intermetallic compounds have traditionally made them less attractive as electrodes for room temperature LiMBs (*35*).

There are generally two major types of Li alloying reactions, solid-solution/insertion and addition/reconstitution (*37*). The solid-solution reaction is topotactic, and there are no phase or structural changes during the Li insertion or alloying process. Alloying reactions with Mg or amorphous Si are good examples of this process. The addition reaction, on the other hand, involves phase change during the lithiation or alloying process, as is commonly observed for alloying Li with Al, Sn, Sb, and crystalline Si. These changes are the source of the low electrochemical reversibility of lithium battery anodes formed from any of these metals and are thought to be particularly disadvantageous in aprotic liquid electrolytes because they require extensive reconstruction of the mechanically poor SEIs and drive complex volume and phase changes at the anode. It is also known that based on the proportions of Li and Al in a thermally formed LiAl alloy, intermetallic compounds composed of $Li_3Al_2$, $Li_2Al$, and $Li_9Al_4$ can be facilely formed at room temperature. We anticipate that a similarly broad range of intermetallic species is present in the electrochemically formed LiM alloys (*33*). We note, however, that a potential advantage of the thermal alloying process over its electro-forming analog is that complications associated with an interphase formation in the electrolyte solutions used for electro-forming LiM alloys are avoided.

The physical characteristics of the LiAl anodes used in this study are analyzed in detail to systematically characterize their composition, physical/electrochemical properties, and Li migration mechanisms. We focus on LiAl alloys containing 20 wt % Al, which yield a lithium-rich LiAl intermetallic compound. LiAl foils in a broad range of thicknesses can be manufactured from ingots with the desired composition in a simple roll-pressing process performed in an inert environment. LiAl foils with thicknesses of 200 μm and higher were found to be more uniform than their thinner counterparts and are therefore selected for the present study. The x-ray diffraction (XRD) peaks in Fig. 1A provide immediate information about the composition of LiAl alloy. The XRD pattern indicates that Li and the $Li_9Al_4$ intermetallic compound are the dominant species present and that the crystal structures correspond to Li (110) and $Li_9Al_4$ (−121). To verify this conclusion, we compare our observations with expectations based on the LiAl phase diagram shown in fig. S1A. Using the Lever rule, the 80 wt % Li and 20 wt % Al mixture forms a LiAl alloy composed of 73 wt % Li and 27 wt % $Li_9Al_4$ at room temperature. Optical images of 200-μm-thick LiM and LiAl foils are provided in Fig. 1B. LiAl alloy was also interrogated using scanning electron microscopy (SEM) to characterize the surface features of LiAl alloy. Results reported in Fig. 1C are obtained in the secondary electron (SE) mode, which allows the surface of LiAl to be interrogated in detail. The same spot was also scanned using the backscattered electron (BSE) mode to verify the hypothesis as shown in Fig. 1D. As the BSE mode can project a clear contrast based on the atomic number, bright regions are displayed in Fig. 1D for $Li_9Al_4$, and energy-dispersive x-ray spectroscopy (EDX) confirms the presence of Al (see Fig. 1E). Together, these data confirm that LiAl consists of Li and the $Li_9Al_4$ intermetallic compound with Li dominantly in the (110) crystal structure and $Li_9Al_4$ dominantly in the (−121) crystal structure.

Considering our goal is to use the LiAl alloy in electrochemical cells, it is important to understand their structural transitions during lithiation and de-lithiation processes. To analyze changes in the structure of LiAl under practically relevant electrochemical conditions, XRD analysis (see fig. S1B) was used to evaluate structural changes in LiAl after 4 mAh $cm^{-2}$ of Li is stripped and redeposited. The XRD patterns recorded after Li stripping and re-deposition cycles are evidently the same, confirming that the structure of the $Li_9Al_4$ intermetallic compound is unaffected by and during Li migration. We note that the broad intensity bump between 10° and 30° in the XRD profiles is attributed to the presence of Kapton tape used to protect the samples from oxidation under the measurement conditions (*38*). On the basis of these results, we conclude that $Li_9Al_4$ remains electrochemically inactive during electrochemical cycling and, as such, may be regarded as forming a stable substrate for

Downloaded from http://advances.sciencemag.org/ on October 31, 2019

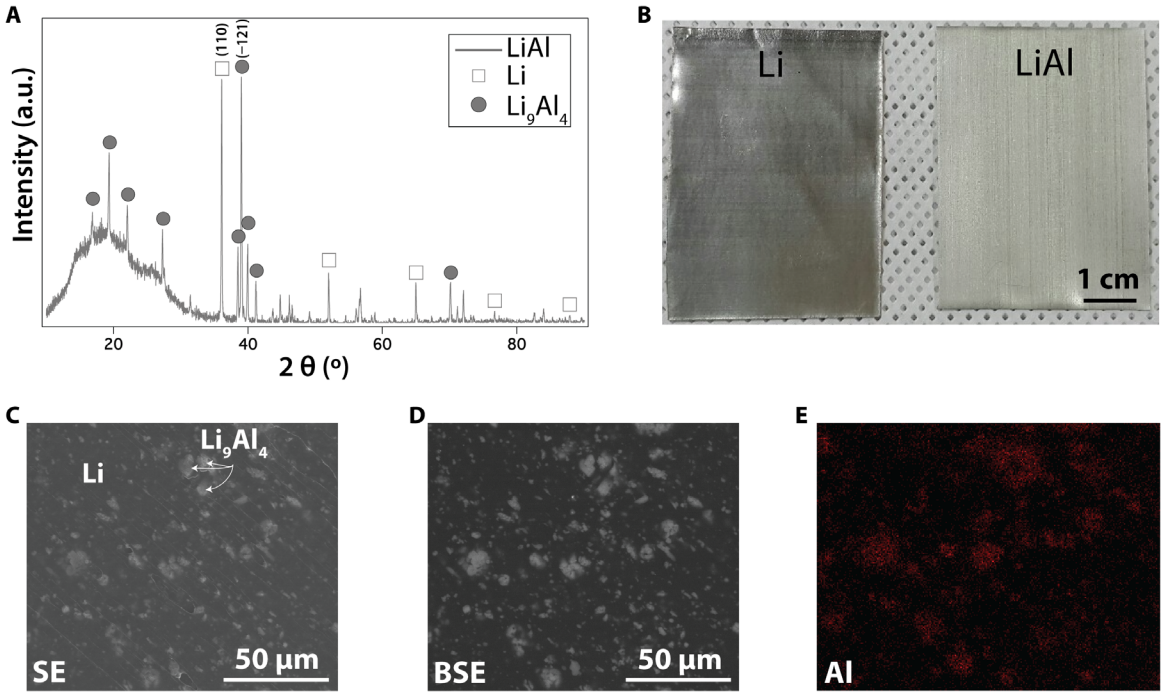


**Fig. 1. Physical characterizations of the LiAl anode.** (**A**) XRD profile of the LiAl anode composed of 80 wt % Li and 20 wt % Al. The dominant XRD peaks correspond to Li (110) and $Li_9Al_4$ (−121) crystal facets. (**B**) Optical images of 200-μm-thick Li and 200-μm-thick LiAl anodes. SEM micrographs of LiAl taken in (**C**) SE mode and (**D**) BSE mode. The dark and bright regions correspond to Li and $Li_9Al_4$ domains in the LiAl anode. (**E**) Corresponding EDX elemental mapping of Al for (C). a.u., arbitrary units.

Li. We attribute this feature of $Li_9Al_4$ to the low Li diffusivity in $Li_9Al_4$ at room temperature.

SEM and focused-ion beam (FIB) analysis were also performed to confirm this phenomenon. The SEM image of 1 mAh $cm^{-2}$ Li-stripped LiAl is shown in fig. S2A. Comparing it with Fig. 1C, it is evident that the Li region is reduced, and more regions of $Li_9Al_4$ are exposed. The elemental mapping of Al shows strong signals around the $Li_9Al_4$ intermetallic compound. Since the SEM image and Al mapping could not identify the properties of LiAl, capacity and cyclic voltammetry (CV) experiments are performed to confirm the electrochemical activity of $Li_9Al_4$, which is discussed later. Further investigation is performed to observe the inner morphologies of $Li_9Al_4$. $Li_9Al_4$ is milled with FIB to observe a cross-sectional image as shown in fig. S2B, and the surface exhibits rock cluster and porous-like morphologies. These findings indicate that the LiAl anode (80 wt % Li and 20 wt % Al proportion) is composed of 73 wt % Li and 27 wt % $Li_9Al_4$ with the major structures of Li (110) and $Li_9Al_4$ (−121) in which $Li_9Al_4$ maintains its structure during and after the Li migration process at ambient temperature.

## First-principles calculations of Li transport for the LiAl anode

To understand the Li migration mechanism for the $Li_9Al_4$ intermetallic compound, Li adsorption and diffusion were investigated for the (−121) facet of $Li_9Al_4$ and compared with that of Li (110). These surfaces are chosen based on the major XRD patterns observed in Fig. 1A. We will initially ignore the effect of chemical changes to the Li/electrolyte interface in characterizing adatom transport; we will refine this assumption later by considering the effect of a well-defined ASEI on LiAl on the conclusions we reach. To investigate the surface of the LiAl anode, we used a slab model–based density functional theoretical (DFT) analysis to perform first-principles calculations for the binding energies for Li (110) and $Li_9Al_4$ (−121). Among the possible adsorption sites for Li, such as hollow, top, and bridge on the top layer of the Li (110) surface, the hollow sites were found to be the most stable. Computing the binding energy of Li for a targeted surface using the following expression

$$E = E_{\text{total}} - [E_{\text{Li}} + E_{\text{surface}}]$$

yields a value of −1.40 eV as seen in Fig. 2A, which agrees with the binding energy value reported by Zhang and co-workers (*39*). Here, $E_{\text{total}}$, $E_{\text{Li}}$, and $E_{\text{surface}}$ are the total energy of the surface after the Li adsorption, the energy of a single Li atom, and the energy of the surface before Li adsorption, respectively. The DFT analysis also reveals that adsorbing Li atoms have a tendency to form multimer clusters on the LiM surface (*40*). The highest binding energy is observed for $Li_2$, and the calculated binding energy (see table S1) is a nonmonotonic function of cluster size, with $Li_2$ (−2.75 eV) > $Li_3$ (−1.68 eV) > Li (−1.40 eV).

This finding provides important insight into Li adatom coverage of the Li (110) surface, indicating that clustering of Li dominates over the uniform binding, which could potentially drive dendritic/mossy depositions of Li widely reported at current densities well below the diffusion limiting current for the LiM anode.

To compute the binding energy of Li on the $Li_9Al_4$ (−121) surface, surface scans were first performed using a vector sum method to determine the possible and most favorable Li adsorption sites. The method is attractive because it incorporates contributions from the surface and subsurface atoms. A total of 44 inequivalent adsorption sites are sampled in a scan, and upon DFT relaxation on each of these 44 configurations containing the adsorbed Li atom over the $Li_9Al_4$ (−121) surface, the three

Downloaded from http://advances.sciencemag.org/ on October 31, 2019

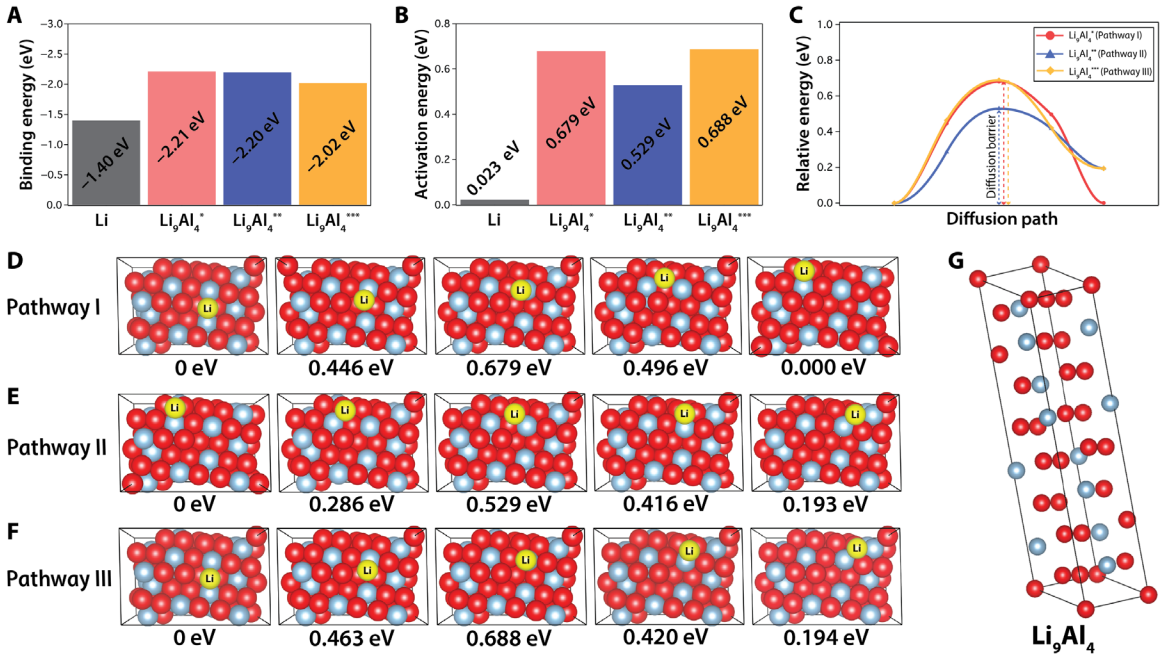


**Fig. 2. First-principles calculations for Li binding energies for the LiAl anode.** (**A**) Binding energy of Li adatoms on Li (110) and $Li_9Al_4$ (−121) surfaces at three stable energy minima of $Li_9Al_4^*$, $Li_9Al_4^{**}$, and $Li_9Al_4^{***}$. (**B**) Activation energy barrier for Li adatom surface diffusion on Li (110) and $Li_9Al_4$ (−121) for three minimum energy pathways, pathway I, pathway II, and pathway III, corresponding to the three stable energy minima of $Li_9Al_4^*$, $Li_9Al_4^{**}$, and $Li_9Al_4^{***}$. The minimum energy pathway is the lowest energy path, connecting two energy minima on the potential energy surface. Theoretical scans over the whole surface were performed to find the energy minima and to identify the three lowest-energy stable sites for $Li_9Al_4$. (**C**) Diffusion paths for Li on the $Li_9Al_4$ (−121) surface at three stable energy minima of $Li_9Al_4^*$, $Li_9Al_4^{**}$, and $Li_9Al_4^{***}$. Top view of the atomic arrangement of Li and Al atoms on the $Li_9Al_4$ (−121) surface to visualize the Li migration on $Li_9Al_4$ (−121) along (**D**) pathway I, (**E**) pathway II, and (**F**) pathway III. The energy values at the bottom of each image are the relative energies calculated with respect to the energy at the initial stable configuration. The initial configuration is the first energy minima from where the Li migration initiates. For the reference, the energy at the first minima is considered as 0 eV. Red and light blue spheres are Li and Al atoms, respectively, and the highlighted yellow sphere is the migrating Li adatom along the minimum energy pathways. (**G**) The atomic arrangement of Li and Al atoms in the unit cell of $Li_9Al_4$.

most stable configurations with binding energies of −2.21, −2.20, and −2.02 eV are identified (Fig. 2A). The higher binding energy values of unclustered Li adsorbed on $Li_9Al_4$ as compared to Li on Li (110) are obvious and notable. We next compare these values to the corresponding binding energies for Li clusters on $Li_9Al_4$ (−121). As shown in table S1, the binding energy of the $Li_2$ cluster on $Li_9Al_4$ (−121) makes this cluster the least probable, and the calculated binding energy (−1.58 eV) is substantially lower than those of $Li_2$ on Li (110) and of Li on $Li_9Al_4$ (−121). The DFT calculations reveal further that upon binding to $Li_9Al_4$ (−121), $Li_2$ clusters break apart to form noninteracting Li adatoms on the $Li_9Al_4$ surface. The bond length between the Li-Li adatoms is found to increase substantially from 2.57 to 4.26 Å, indicating that there is almost no interaction between individual Li adatoms. The results reported in table S1 show further that the binding energy of Li on $Li_9Al_4$ is the maximum among the Li clusters, meaning that in comparison to the Li (110) surface, Li clustering is not favored on the $Li_9Al_4$ (−121) surface.

It is conventionally thought that surface diffusion of Li adatoms plays a crucial role in the uniformity of Li electrodeposition at the LiM anode. Here, we study such surface diffusion behavior of Li on the LiAl anode using a climbing image nudged elastic band (CI-NEB) approach. The strategy is based on the modified nudged elastic band method, in which optimization of the configurations between two stable energy minima is correlated with the spring constant and force acting in the perpendicular direction to the elastic band so that one of the configurations climb up to the highest saddle point (*41*). The activation energy, defined here as the threshold energy required by adsorbing the Li atom to migrate from one energy minima to the other nearby minima, is estimated from the energy maxima across the diffusion paths of the adsorbed Li atom. This definition means that it always has a positive value that is independent of the exothermic or endothermic nature of the process. Motivated by the results from the previous section, the diffusion path analysis for Li on the Li (110) surface focuses on transport between adjacent hollow sites, where a hollow-bridge-hollow pathway is followed by Li adatoms as shown in fig. S3. The bridge site corresponds to the transition state with the activation energy of 0.023 eV. The inset atomic arrangements presented at each of the data points in fig. S3 are the corresponding system configurations of the migrating Li, the yellow atom, on the Li (110) surface. The atomic structure profiles along the minimum energy pathway followed by the migrating Li on the Li (110) surface in fig. S3 are the immediate optimized configuration of the adsorbed Li atom on the Li (110) surface. The top view of the initial and final energy minima in the activation barrier profile in fig. S3 corresponds to the adsorption of Li on the hollow site, while the highest energy point shows the adsorption of Li on the bridge site on the Li (110) surface, which provides a clear visualization of the hypothesis on the hollow-bridge-hollow pathway followed by Li on the Li (110) surface. The calculated activation energy for Li on the Li (110) surface is 0.023 eV, as shown in Fig. 2B, which is in agreement with the reported value (*42*) and comparable to the energy barrier (0.03 eV) reported from joint DFT calculations for Li adatom diffusion on surfaces such as LiBr (*43*) that facilitate fast Li adatom mobilities in liquid electrolytes. The calculated activation energy is also evidently below the thermal energy

Downloaded from http://advances.sciencemag.org/ on October 31, 2019

(0.025 eV) at room temperature. This means that Li diffusion on the Li (110) surface is essentially unhindered and instantaneous.

To compare the activation energies of the migrating Li across the $Li_9Al_4$ (−121) surface with that of the Li (110) surface, the atomic configurations for Li on $Li_9Al_4$ corresponding to the optimized atomic structure profiles of the three most stable energy minima are used. Thus, the diffusion paths of the migrating Li on the surface of $Li_9Al_4$ generate a maximum of three possible pathways, which are named pathway I, pathway II, and pathway III. The diffusion paths of Li based on the three pathways are shown in Fig. 2C. The corresponding activation energies reported in Fig. 2B for pathways I, II, and III are 0.679, 0.529, and 0.688 eV, respectively. The atomic arrangements of the configurations adopted by migrating Li on $Li_9Al_4$ (−121) are shown in Fig. 2 (D to F), where the leftmost images represent the initial state of adsorbed Li. The energy values for each configuration during the course of Li migration with respect to the reference stable minima are mentioned below for each of the images. For pathway I, the metastable configurations for the migrating Li in between the initial and final energy minima have energy values of 0.446, 0.679, and 0.496 eV with an activation energy of 0.679 eV. For pathway II, the energy values for the metastable states are 0.286, 0.529, and 0.416 eV with an activation energy of 0.529 eV. For pathway III, the corresponding energy values are 0.463, 0.688, and 0.420 eV with an activation energy of 0.688 eV. The atomic structures for the bulk configuration of elemental Li and Al in $Li_9Al_4$ are shown in Fig. 2G, which can be used to model the surface configuration of $Li_9Al_4$ (−121).

The rate of the Li surface diffusion can be related to the activation energy using the analytical Arrhenius equation

$$k = Ae^{-Ea/RT}$$

where $k$ is the rate constant, $A$ is the frequency factor that depends on the hopping frequency of the migrating Li adatoms, $Ea$ is the activation energy, $R$ is the gas constant of 8.3145 J $K^{-1}$ $mol^{-1}$, and $T$ is the absolute temperature in kelvin. The magnitude of the activation energy values deduced from the calculations therefore implies that among the multitude of possible surface pathways available for Li adatom diffusion, the surface diffusion of Li on $Li_9Al_4$ is not spontaneous and is likely far slower than that on Li (110). Thus, in the case of Li on the Li (110) surface, the combination of a low binding energy, an enhanced propensity to form clusters, and a low activation energy barrier for adatom transport could explain the tendency to form nonuniform mossy deposits at currents below the diffusion limit where dendritic electrodeposition of all metals is a fundamental consequence of the hydrodynamic instability known as electroconvection (*14*). In contrast, in the case of the $Li_9Al_4$ (−121) surface, the combination of higher binding, low propensity to form adatom clusters, and higher surface diffusion barriers would favor a more uniform Li deposition and a lower tendency for migration of adatoms from adsorption sites to regions of faster growth. We evaluate these ideas next by interrogating the electrochemical and physical characteristics of Li electrodeposits at the LiAl anode.

## Morphological and electrochemical features of the LiAl anode

The morphology and electrochemical features of the LiAl anode are investigated using LiAl|LiAl symmetric and LiAl|NCM811 full cells. Figure 3 (A to D) reports SEM surface morphologies of LiAl when 1, 2, 3, and 4 mAh $cm^{-2}$ Li, respectively, are stripped from the LiAl electrodes. In Fig. 3 (A to D), the Li region as indicated in Fig. 3A in each of the figures is gradually disappearing with respect to increasing Li stripping amount on the LiAl anode (see also fig. S2A). According to Fig. 2A, $Li_9Al_4$ has the higher binding energy for Li, and therefore, biased Li deposition has been observed around $Li_9Al_4$. Figure 3 (E and F) shows the SE and BSE mode SEM images obtained when 1 mAh $cm^{-2}$ is redeposited on a LiAl electrode previously stripped of 1 mAh $cm^{-2}$ of Li. It is apparent that Li tends to deposit and grow around $Li_9Al_4$. Figure 3G shows the corresponding SE mode SEM image obtained when 4 mAh $cm^{-2}$ Li is redeposited on a LiAl electrode previously stripped of 4 mAh $cm^{-2}$ Li. The results show that more compact Li deposits are observed at the $Li_9Al_4$ intermetallic compound. In Fig. 3H, the SEM image is taken at the same position using the BSE mode to facilitate contrast between the Li electrodeposits and $Li_9Al_4$. Comparing these results to the Li deposition observed for the LiM electrode (fig. S4), it is clear that more compact Li deposits are obtained with the LiAl electrode, as shown in Fig. 3G. This Li deposition behavior is in agreement with expectations based on our analysis of Li adatom binding and transport at Li and $Li_9Al_4$ discussed in the previous section. In other words, the high activation energy of $Li_9Al_4$, which presents an irregular and nonintercalating surface to the arriving $Li^+$, but which strongly binds the reduced Li adatoms, stabilizes the Li electrodeposition as observed in Fig. 3G. This observation also leads us to conclude that while the binding energy can provide insights into the Li affinity to the surface, it must be coupled with information on adatom surface diffusion to fully understand the evolution of morphology at the LiM electrode. Thus, while a low activation energy for Li transport may be favored for Li deposition at homogeneous electrode surfaces formed by two-dimensional (2D) materials such as graphene and $MoS_2$ (see the discussion below), with significant Li intercalation capability, higher activation energy is potentially favored to stabilize Li electrodeposition at heterogeneous surfaces without Li intercalation capability (see fig. S2B). The hypothesis is that surfaces with high binding energy for Li are needed to strongly adhere Li during the Li migration at that surface, but high or low activation energy of Li is conditionally needed with respect to the lithium deposition substrate surface characteristics. The high activation energy is potentially favored for the rough and nonintercalating surfaces to stabilize the Li migration by preventing the forced surface diffusion of Li to the thermodynamically favorable sites. One common example for this case would be Li migration occurring at a flat versus 3D/tortuous structured Cu substrate. It is clear that Cu has low surface diffusion of Li as Li does not interact with Cu and forms dendrites, and because of the low surface diffusion of Li on Cu, having 3D/porous structures on Cu helps to prolong the life span of the LiM anode not only by providing distributed point charges and ion flux but also because of the slow surface diffusion of Li on 3D/porous Cu. In the other case, the low activation energy is potentially favored for the uniform and intercalating surfaces to provide facilitated surface diffusion of Li. The resulting surfaces are free of the biased favorable diffusion sites that help uniform overplating of Li and hinder the formation of Li aggregates. This is often the reason why there are limited numbers of 2D high–surface area material–based Li deposition platforms with intercalation capability reported for the LiM anode. Therefore, the high activation energy of $Li_9Al_4$, which has rough and nonintercalating surfaces, along with the high binding energy of Li helps to stabilize Li migration as observed in Fig. 3G.

The reversibility of the Li migration processes at the anode is a key determinant of the success of rechargeable batteries based on LiM anodes. To observe the reversibility of the LiAl anode, Li stripping

Downloaded from http://advances.sciencemag.org/ on October 31, 2019

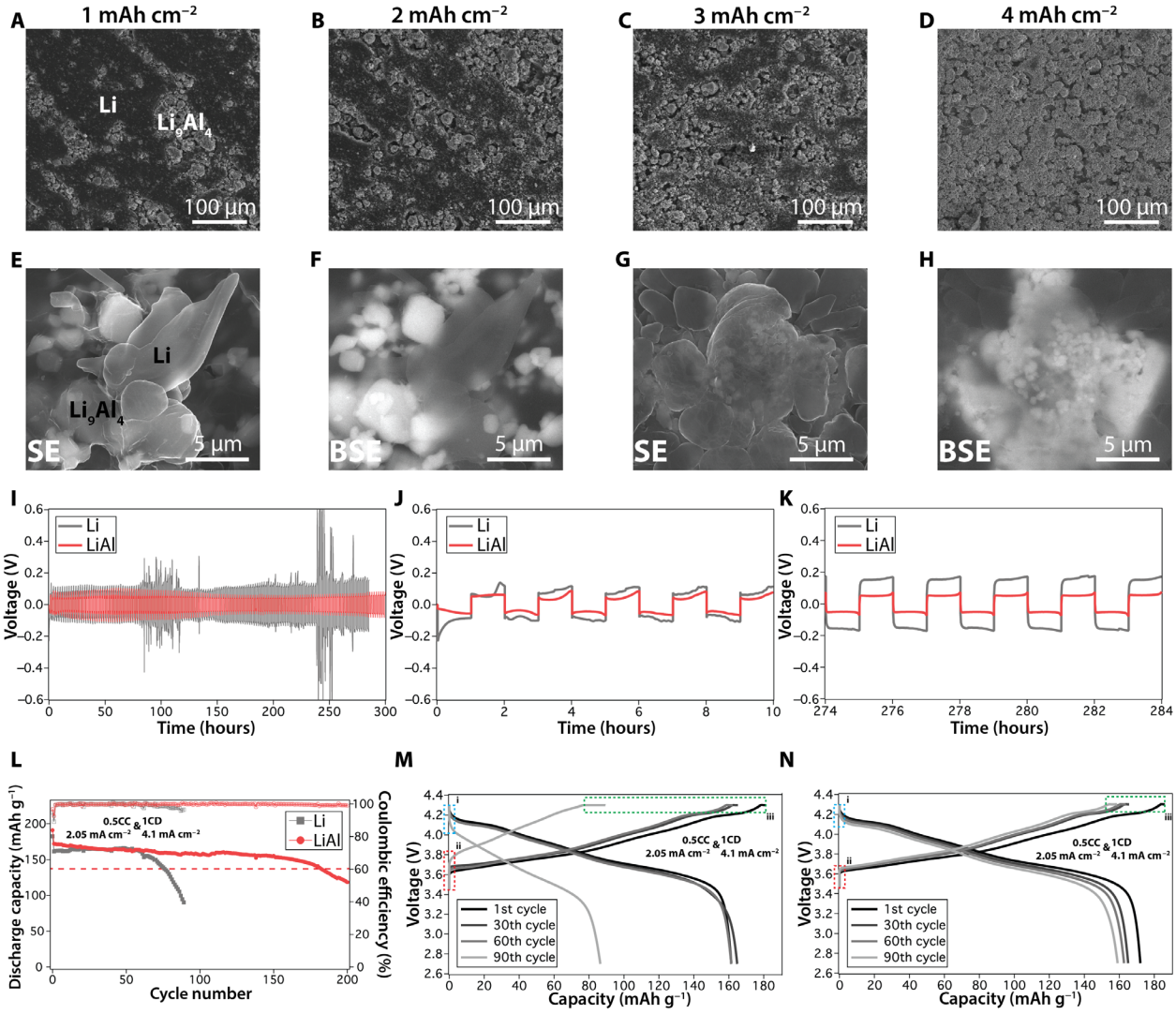


**Fig. 3. Electrochemical analysis for the LiAl anode.** Surface morphologies of the LiAl anode after galvanostatic stripping of Li in LiAl|LiAl symmetric cells at the fixed current density of 1 mA $cm^{-2}$ and for the different amounts of charge passed: (**A**) 1 mAh $cm^{-2}$, (**B**) 2 mAh $cm^{-2}$, (**C**) 3 mAh $cm^{-2}$, and (**D**) 4 mAh $cm^{-2}$. SEM images of Li electrodeposits on LiAl when 1 mAh $cm^{-2}$ of Li is first stripped followed by 1 mAh $cm^{-2}$ Li deposition on $Li_9Al_4$ taken in (**E**) SE mode and (**F**) BSE mode. SEM images of Li electrodeposits on LiAl when 4 mAh $cm^{-2}$ of Li is first stripped followed by 4 mAh $cm^{-2}$ Li deposition on $Li_9Al_4$ taken in (**G**) SE mode and (**H**) BSE mode. (**I**) Galvanostatic Li migration voltage profiles measured for Li|Li and LiAl|LiAl symmetric cells at a fixed current density of 1 mA $cm^{-2}$ and a capacity of 1 mAh $cm^{-2}$. Magnified Li migration voltage profiles in (I), (**J**) from 0 to 10 hours and (**K**) from 274 to 284 hours. (**L**) Cycling profiles based on the discharge capacities (filled symbols) and Coulombic efficiencies (open symbols) for Li|NCM811 and LiAl|NCM811 full cells at C rate charging (CC) and C rate discharging (CD) of 0.5 CC and 1 CD with a voltage window of 2.7–4.3 V. (**M**) Corresponding voltage profiles for the Li|NCM811 full cell from (L) for the 1st to the 90th cycle. Region i represents the initial voltage profiles during the cell discharge. Region ii represents the initial voltage profiles during the cell charge. Region iii represents the voltage profiles at the constant voltage charging. The current densities for charging and discharging rates are 2.05 mA $cm^{-2}$|0.5 CC and 4.1 mA $cm^{-2}$|1 CD, with a cathode areal capacity of 4.1 mAh $cm^{-2}$. (**N**) Corresponding voltage profiles of the LiAl|NCM811 full cell from (L) for the 1st to the 90th cycle. Region i represents the initial voltage profiles during the cell discharge. Region ii represents the initial voltage profiles during the cell charge. Region iii represents the voltage profiles at the constant voltage charging. The current densities for charging and discharging rates are 2.05 mA $cm^{-2}$|0.5 CC and 4.1 mA $cm^{-2}$|1 CD, with a cathode areal capacity of 4.1 mAh $cm^{-2}$.

and plating experiments were performed in Li|Li and LiAl|LiAl symmetric cells under galvanostatic conditions at a current density of 1 mA $cm^{-2}$ and a capacity of 1 mAh $cm^{-2}$. Voltage profiles deduced from these experiments are reported in Fig. 3I. The profiles for LiAl|LiAl symmetric cells are seen to exhibit stable and well-maintained shapes for more than 300 hours, with no evidence of sudden reductions associated with internal electrode shorting. On the other hand, the voltage profiles observed for Li|Li symmetric cells exhibit sudden and irregular voltage spikes, and there is a gradual increase of Li migration potential during cycling. In Fig. 3J, the voltage profile for the LiAl symmetric cell is zoomed in for 0 to 10 hours to observe the initial stages of Li electrodeposition characteristics. Again, it is seen that the cells exhibit stable cycling profiles essentially from the beginning of the experiments, whereas the Li symmetric cell exhibits obvious instability from the inception. This gradual change of the voltage profile is dominated by the evolution of the interfacial impedance of the electrodes since no internal shorting of the electrodes, where the voltage should sharply drop, is observed. The Li foil often comes with passivated surfaces,

Downloaded from http://advances.sciencemag.org/ on October 31, 2019

mainly native oxides, because of its high chemical reactivity under ambient environments. Thus, high interfacial impedance of Li is often observed, and as the passivation layers break during the dendritic Li electrodeposition process, freshly electrodeposited Li dendrites are exposed to the electrolyte, decreasing the interfacial impedance by the increased surface area and the absence of the native oxide layers. This explains the voltage fluctuation of Li symmetric cells in the beginning. For LiAl electrodes, LiAl is composed of Li and the $Li_9Al_4$ intermetallic compound as shown in Fig. 1. As the $Li_9Al_4$ intermetallic compounds has a lower reactivity than Li, LiAl tends to maintain better surface features compared to Li. In fig. S5, Nyquist plots are shown for LiAl and Li symmetric cells, and further impedance changes are observed for the symmetric cells assembled with 1-month-exposed LiAl (fig. S5A) and Li (fig. S5B) electrodes under dry atmosphere at a dew point around −70°C. The Nyquist plots show that the LiAl symmetric cell has lower impedance than the Li symmetric cell. One other possible explanation is that the surface features are well maintained as LiAl exhibits a shinier color than Li as observed in Fig. 1B. Also, a higher increase of the impedance is observed for the symmetric cells with the exposed Li electrodes compared to the exposed LiAl electrodes (fig. S5), which further supports the idea that the LiAl electrode is less reactive and maintains better surface characteristics.

By confirming stabilized and reversible Li migration processes for LiAl electrodes, LiAl is used as the anode in the full cell to perform in-depth electrochemical studies with the 4.1 mAh $cm^{-2}$ NCM811 cathode. Figure 3L shows the cycling performance of Li|NCM811 and LiAl|NCM811 full cells. With the LiAl anode, the cycle life of the full cell has almost been doubled compared to the full cell with the LiM anode. The extension of the cycle life for the LiAl|NCM811 cell is due to the stable and reversible Li migration during the charge/discharge process. As shown in fig. S6, compact and uniform Li deposits are shown for the LiAl anode from the full cell where the full cell with the LiM anode shows sparsely deposited Li due to the unstable Li migration. As the LiAl anode allows stable Li migration, this phenomenon correlates to compact Li deposition and to stable Li growth by achieving well-preserved SEIs at the anode, which should also translate to well maintained interfacial impedance of the LiAl anode during cell cycling. Figure 3 (M and N) shows the voltage profiles of Li|NCM811 and LiAl|NCM811 full cells for the 1st, 30th, 60th, and 90th cycle. To compare the voltage profiles from these two cells, we compared the charge/discharge profiles at the indicated cycles, as shown in fig. S6C. Regions i, ii, and iii are indicated in the profiles to provide clear comparisons for the impedance evolution. Regions i, ii, and iii represent the initial voltage profiles during the galvanostatic cell discharge, the initial voltage profiles during the galvanostatic cell charge, and the voltage profiles at the constant voltage charging, respectively. In Fig. 3M, the voltage drops at region i, and the voltage increase at region ii becomes steeper as the cycle number increases. Also, in region iii, constant voltage charging tails become longer as cycle number increases. These changes are due to the increase of the internal impedance, mainly at the anode. For regions i and ii, steeper changes in the discharge and charge voltages are gained by the increased internal impedance, which also decreases the cell capacity at the fixed cycling C rates due to the decreased power density of the cell. Region iii further confirms this impedance limit by yielding a higher portion of the constant voltage charging compared to the previous cycle.

As charging and discharging processes are controlled by the cutoff voltage values, the rate that the voltage galvanostatically reaches the limit is dependent on cell impedance. Hence, with a constant cycling C rate, enlargement of constant voltage charging (region iii) and steep voltage changes during discharging and charging (regions i and ii) are attributed to the increase of cell impedance, demonstrating that the cell failure is caused by impedance buildup, not by the active material depletion or internal short circuit. Thus, comparing the voltage profiles of Fig. 3M with those of Fig. 3N, it can be seen that regions i, ii, and iii are stabilized for the LiAl|NCM811 full cell under the same cycling conditions and cycle numbers. In Fig. 3N, the discharging and charging voltage profiles remain almost constant, indicated by regions i and ii, and the constant voltage charging (region iii) remains almost unchanged. These findings mean that the impedance buildup is delayed and Li migration upon cycling is stabilized by the use of the LiAl anode in the full cell, therefore allowing prolonged cycle life, compared to the full cell with the LiM anode. Therefore, these prospective results provide support for using LiAl anode as opposed to the conventional LiM anode for LiMBs. However, the LiAl anode requires improvement to provide higher electrochemical reversibility and better Li migration.

### Li migration analysis for $MoS_2$ LBASEI

Our analysis up to this point has ignored the effect of the chemical instability of Li in contact with all (liquid, quasi-liquid, and solid state) electrolytes and the importance of a well-formed SEI on Li to achieve electrochemical stability of the LiM anode. In particular, we have so far ignored the role that SEI plays in regulating the binding strength, transport properties, and stability of Li migration at the LiM anode/electrolyte interface. With the specific aim of testing our hypothesis under more realistic conditions for a practical LiM anode, we investigated the effect of a well-defined $MoS_2$ LBASEI deposited on LiAl. The choice of $MoS_2$ is motivated by a recent study by Choi and co-workers (*44*), which shows that application of a low-dimensional $MoS_2$ protective layer on Li is effective in stabilizing cycling of LiMBs in liquid electrolytes. The atomic sputtering process commonly used for the application of 2D $MoS_2$ on LiM is unfortunately cumbersome and incompatible with large-scale, low-cost electrode fabrication. Here, we consider an alternative LBS approach that allows uniform and compact $MoS_2$ coatings to be transferred to the LiAl anode. The fabrication process is straightforward as the LBS method is applied under ambient conditions to create $MoS_2$ LBASEI, which is transferred onto the LiAl anode via roll-pressing in a dry atmosphere with a dew point below −70°C. Optical images of the prepared $MoS_2$ LiAl anode are provided in fig. S7.

To elucidate the effect of $MoS_2$ LBASEI on Li adatom binding and transport on the LiAl surface, we used the same first-principles approach used in the previous sections to study the structure, binding energies, and surface diffusivity of Li adatoms. It is known that $MoS_2$ exists in two primary polymorphs: the 2H ($MoS_2$ 2H) and T ($MoS_2$ T) phases of $MoS_2$. The $MoS_2$ 2H phase exhibits a trigonal prismatic symmetry and displays semiconducting properties, while the $MoS_2$ T phase has octahedral symmetry and exhibits metallic properties (*44*, *45*). Our DFT calculations show (see Fig. 4A) that the $MoS_2$ 2H is energetically most stable. To investigate the possibility for the structure transformations of $MoS_2$ during lithiation, the free energies of 2H and T phases of $MoS_2$ were calculated with respect to the degree of lithiation or equivalently the lithium concentration for $MoS_2$. The free energy refers to the Helmholtz free energy defined as the total internal energy of the system at absolute zero temperature and at absolute zero entropy of the system. To study the Li adsorption behavior on $MoS_2$, various possible adsorption sites of Li are investigated, such as the top of

Downloaded from http://advances.sciencemag.org/ on October 31, 2019

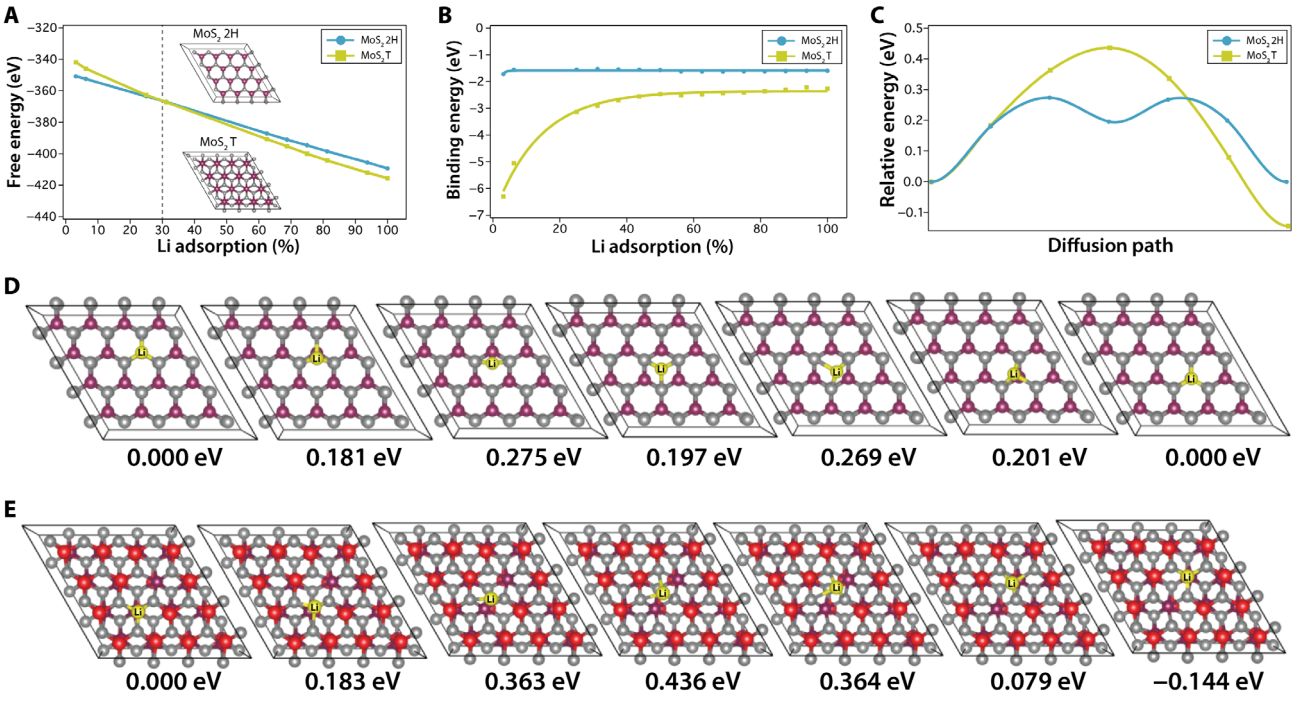


**Fig. 4. First-principles calculations for $MoS_2$ LBASEI.** (**A**) In situ free-energy transition of $MoS_2$ 2H to $MoS_2$ T with respect to Li concentrations. The inset images are the atomic models of the unit cells of $MoS_2$ 2H and $MoS_2$ T. The vertical dashed line represents the transition state of 2H to T phase of $MoS_2$ at 30% lithiation, which is the critical Li concentration in which the phase transition occurs. (**B**) Binding energy of Li based on the Li concentrations for $MoS_2$ 2H and $MoS_2$ T. (**C**) Diffusion paths of Li on the surfaces of $MoS_2$ 2H and lithiated $MoS_2$ T along the t-h-t pathway, where t is the top site of the Mo atom and h is the hollow site in the hexagonal ring of Mo and S atoms. Top view of the atomic arrangement of Mo and S atoms in the $MoS_2$ surface to visualize Li migration on (**D**) $MoS_2$ 2H and (**E**) lithiated $MoS_2$ T along the t-h-t pathway. The energy value below each image is the relative energy with respect to the initial configuration for corresponding phases of $MoS_2$. The initial configuration is the first stable site from where Li migration initiates. Plum, light purple, and red spheres are Mo, S, and Li atoms, respectively, and the highlighted yellow sphere is the migrating Li atom along the minimum energy pathway.

Mo, top of S, bridge, and hollow sites. The atomic structure of $MoS_2$ 2H and $MoS_2$ T and the possible adsorption sites of Li are shown in fig. S8. The computational results show that the top of the Mo atom has the most favorable binding site for Li as it provides the minimum energy configuration compared to the other adsorption sites. Similarly, for $MoS_2$ T, the top of the Mo atom is the most favorable Li binding site. As Mo atoms in $MoS_2$ can accommodate Li atoms on both sides of the atomic layer, $MoS_2$ works as an effective platform and channel to and for the flow of Li during Li migration. The DFT results show that lithiation produces the phase transition from a $MoS_2$ 2H– to a $MoS_2$ T–dominant structure (see Fig. 4A). The inset atomic configurations in the figure show the unit cells of $MoS_2$ 2H and $MoS_2$ T. At a critical Li concentration corresponding to 30% lithiation, indicated by the dashed vertical line in Fig. 4A, the in situ phase transition occurs from $MoS_2$ 2H to $MoS_2$ T. Above the critical Li concentration, $MoS_2$ T becomes the most favorable phase for the lithiated $MoS_2$ (*46*). It is to be noted that for the lithiation of $MoS_2$, both sides of the surface are considered for the Li adsorption process.

The binding energy of Li on $MoS_2$ was calculated on the basis of the Li concentration for both 2H and T phases. At the beginning of the Li adsorption process, the binding energies of $MoS_2$ 2H and $MoS_2$ T are determined to be −1.72 and − 6.30 eV, as shown in Fig. 4B. Since $MoS_2$ T is not the energetically stable phase at the beginning of the lithiation process, higher energy is required to facilitate the process of Li adsorption, as compared to the $MoS_2$ 2H phase, which would make the initial adsorption rate of Li on $MoS_2$ T slow. Any potential beneficial effects associated with the strong binding will therefore not be realized at the beginning of the lithiation process. The binding energy of Li on the unlithiated $MoS_2$ 2H (−1.72 eV) can also be compared with the earlier values for Li (−1.40 eV) and $Li_9Al_4$ (−2.21 eV). This implies that faster Li adsorption but weaker Li affinity on $MoS_2$ than on $Li_9Al_4$ would be expected. It also means that slower Li adsorption but higher Li affinity would be expected at $MoS_2$ than at Li. As the lithiation of $MoS_2$ proceeds, however, the adsorption of Li on the lithiated $MoS_2$ changes. The binding energy of Li on lithiated $MoS_2$ 2H (the less stable phase of the lithiated $MoS_2$) is −1.55 eV, and the binding energy of Li on lithiated $MoS_2$ T (the more stable phase of the lithiated $MoS_2$) is −2.46 eV. The latter value is more negative than the binding energy for $Li_9Al_4$, meaning that the Li is more strongly adhered to the surface of lithiated $MoS_2$ during Li migration. The importance of this result is amplified by the fact that $MoS_2$ LBASEI on Li will be naturally lithiated by the contact with the LiM as will be discussed later, meaning that even during the earliest stages of lithiation, $MoS_2$ T would be the more dominant phase present in the ASEI and that this phase will persist until lithiation ends.

The surface diffusion of Li adatoms on $MoS_2$ was studied using the same CI-NEB method described previously. For the Li binding on $MoS_2$, the top of Mo is the most favorable binding site followed by the hollow site. Hence, the path followed by Li diffusion must be the top of Mo–hollow–top of Mo (*47*). The diffusion paths of the migrating Li on the unlithiated and lithiated $MoS_2$ surfaces, corresponding to $MoS_2$ 2H and lithiated $MoS_2$ T surfaces based on the free energy

Downloaded from http://advances.sciencemag.org/ on October 31, 2019

provided in Fig. 4A, are shown in Fig. 4C. For the unlithiated $MoS_2$, $MoS_2$ 2H, local energy minima are observed at the hollow site during Li migration, which can be explained by the hollow site having the second minimum energy value compared to the top of the Mo site. In between the hollow and top sites, the metastable transition state is observed. The top view of the metastable states in the course of Li migration on the surface of $MoS_2$ 2H is shown in Fig. 4D, where each configuration (left to right) shows the path followed by the migrating Li, the yellow atom. The relative energy values of each configuration with respect to the initial stable energy minima are 0.181, 0.275, 0.197, 0.269, and 0.201 eV, with an activation energy of 0.275 eV. The activation energy for Li migration on $Li_9Al_4$ is in the range of 0.529 to 0.688 eV owing to the three most probable pathways, as discussed earlier. The smaller value of the activation energy for $MoS_2$ 2H indicates that a smaller amount of energy is required for Li adatom diffusion, as compared to $Li_9Al_4$. As the lithiation of $MoS_2$ continues, $MoS_2$ T is the dominant substrate and similar Li migration paths are followed as the top of Mo–hollow–top of Mo. However, because of the octahedral geometry of the lithiated $MoS_2$ T, one of the two hexagonal ring patterns formed by the Mo and S slides toward the centroid of the other hexagonal ring pattern, as shown in fig. S8. Therefore, no local energy minima are observed for Li diffusion on the lithiated $MoS_2$ T, as shown in Fig. 4C. The top view of the atomic configurations in the course of Li migration on the lithiated $MoS_2$ T is shown in Fig. 4E. The relative energy values of the metastable configuration with respect to the initial stable energy minima are 0.183, 0.363, 0.436, 0.364, and 0.079 eV, with an activation energy of 0.436 eV, which are again smaller than the activation energies of $Li_9Al_4$ (0.529 to 0.688 eV). As $MoS_2$ involves the Li intercalation process during Li migration, low activation energy for Li transport helps to facilitate the intercalation process, resulting in stable Li migration as Li overplates. Also, the uniform surfaces of $MoS_2$ may facilitate stable Li migration. We therefore conclude that the lithiated $MoS_2$ LBASEI, composed primarily of lithiated $MoS_2$ T, exhibits a combination of a high Li binding energy, molecular smoothness, and low barrier to Li adatom diffusion, which favors efficient binding of Li and transport away from the electrode/electrolyte interface, which favors stable and reversible Li migration of the $MoS_2$ LiAl anode.

### Morphological and electrochemical features of the $MoS_2$ LiAl anode

The low standard redox potential of Li (−3.04 V versus SHE) and its chemical reactivity drive spontaneous lithiation of $MoS_2$ LBASEI in contact with the LiAl anode (*48*). SEM analysis of the $MoS_2$ LiAl anode confirms that $MoS_2$ forms a compact, uniform coating on LiAl (see Fig. 5A). EDX elemental mappings of Mo and S atoms shown in Fig. 5B confirm the chemical uniformity of $MoS_2$ LBASEI. The electrochemical reversibility of $MoS_2$ LiAl anodes is investigated in LiAl $MoS_2$|$MoS_2$ LiAl symmetric cells using galvanostatic stripping and plating measurements at a fixed current density of 1 mA $cm^{-2}$. By reversing the polarity of the electrodes every hour, a strip/plate capacity of 1 mAh $cm^{-2}$ was maintained under an approximately square-wave current profile. Figure 5C compares the resultant voltage profiles with the corresponding ones for LiAl|LiAl symmetric cells measured in the same electrolyte and cell running conditions. It is apparent from the figure that the voltage response for the $MoS_2$ LiAl better approximates the square-wave current profile, implying that the minimal new resistances are produced during electrochemical cycling of the symmetric cells. In contrast, LiAl symmetric cells exhibit more complex transient voltage responses, including the appearance of voltage spikes near the beginning and end of each strip/plate cycle, indicative of the complex influences a spontaneously formed SEI has on the Li migration during the stripping and plating processes. In addition, beginning at around 420 hours of the cycling measurements, a steady increase in the peak-to-peak voltage is observed for LiAl symmetric cells, which is a common signature of electrolyte degradation and thickening of the SEI. In contrast, $MoS_2$ LiAl symmetric cells exhibit exceptional stability even after 700 hours of plate/strip cycling. This result reveals that Li migration reversibility has been improved by $MoS_2$ LBASEI for the LiAl anode and that the SEI formed spontaneously on the LiM anode limits reversibility by impedance buildup, as opposed to the formation of the internal short circuits due to dendritic Li deposition.

To analyze Li migration behavior in greater detail, zoomed-in voltage profiles are shown for the first 10 hours (Fig. 5D), the 410th to 430th hours (Fig. 5E), and the 680th to 700th hours (Fig. 5F) after the initial cycling. The results reported in Fig. 5D show very stable potential profiles with $MoS_2$ LiAl where almost no potential fluctuations are found. The voltage profiles of LiAl symmetric cells shown in Fig. 5E exhibit a steep increase of Li migration voltages, indicating the high interfacial resistances of LiAl, whereas the $MoS_2$ LiAl shows stable voltage profiles of up to 700 hours shown in Fig. 5F. These results confirm that smooth Li deposition and dissolution occur during the Li migration process and support our earlier contention that $MoS_2$ LiAl allows highly reversible Li migration.

Results reported in Fig. 5 (G to J) from SEM analysis of $MoS_2$ LiAl electrodes after 1, 2, 3, and 4 mAh $cm^{-2}$ Li deposited onto the electrodes provide clearer physical insights into the morphological features of Li electrodeposits formed by the $MoS_2$ LiAl electrodes. The results show that Li coverage gradually increases with deposition capacity and that the deposits are compact and uniform, consistent with the inferences deduced from the voltage profiles. To investigate the role played by $MoS_2$ LBASEI coating thickness, we characterized the nucleation overpotential of Li on $MoS_2$ LBASEI for different coating thicknesses. In Fig. 5K, the galvanostatic voltage profiles are shown for $MoS_2$ LBASEI, with thickness ranging from 0 to approximately 3 μm, where 0 μm corresponds to a bare Cu substrate. The results show that there is an initial marked reduction from 40 to 10 mV in the Li nucleation overpotential, but that the nucleation overpotential remains essentially unchanged for $MoS_2$ LBASEI thicknesses above 2.04 μm (see Fig. 5L); we, therefore, fixed the thickness of $MoS_2$ LBASEI to 2 μm in the remainder of our studies. The low Li nucleation overpotential observed for $MoS_2$ LBASEI is a consequence of the effectiveness of $MoS_2$ as LBASEI on LiAl and of the fast adatom transport. While it is tempting to attribute these features to the ability of $MoS_2$ to intercalate Li, we note that the normalized capacity of $MoS_2$ LBASEI is calculated by multiplying the time at 0 mV with the applied current density followed by a thickness normalization capacity of 0.094 mAh $cm^{-2}$ $\mu m^{-1}$ to account for the intercalation capacity of $MoS_2$ LBASEI. As this capacity also includes both of the SEI formation and lithiation processes, the Li lost in the SEI formation step would not contribute to the reversible electrode capacity. Considering the small thickness of $MoS_2$ LBASEI used in the study, the contribution to the overall electrode capacity is negligible. For instance, using the capacity of the 4.1 mAh $cm^{-2}$ cathode, the 2-μm-thick $MoS_2$ LBASEI would contribute a storage capacity of at most 2.3% to the anode. As a final step to concretely connect the migration voltage profiles and morphology of Li electrodeposits at the $MoS_2$ LiAl electrodes, we performed large-area SEM scans (fig. S9A) and cross-sectional SEM images (fig. S9, B and C) to fully access the topography of Li electrodeposits.

Downloaded from http://advances.sciencemag.org/ on October 31, 2019

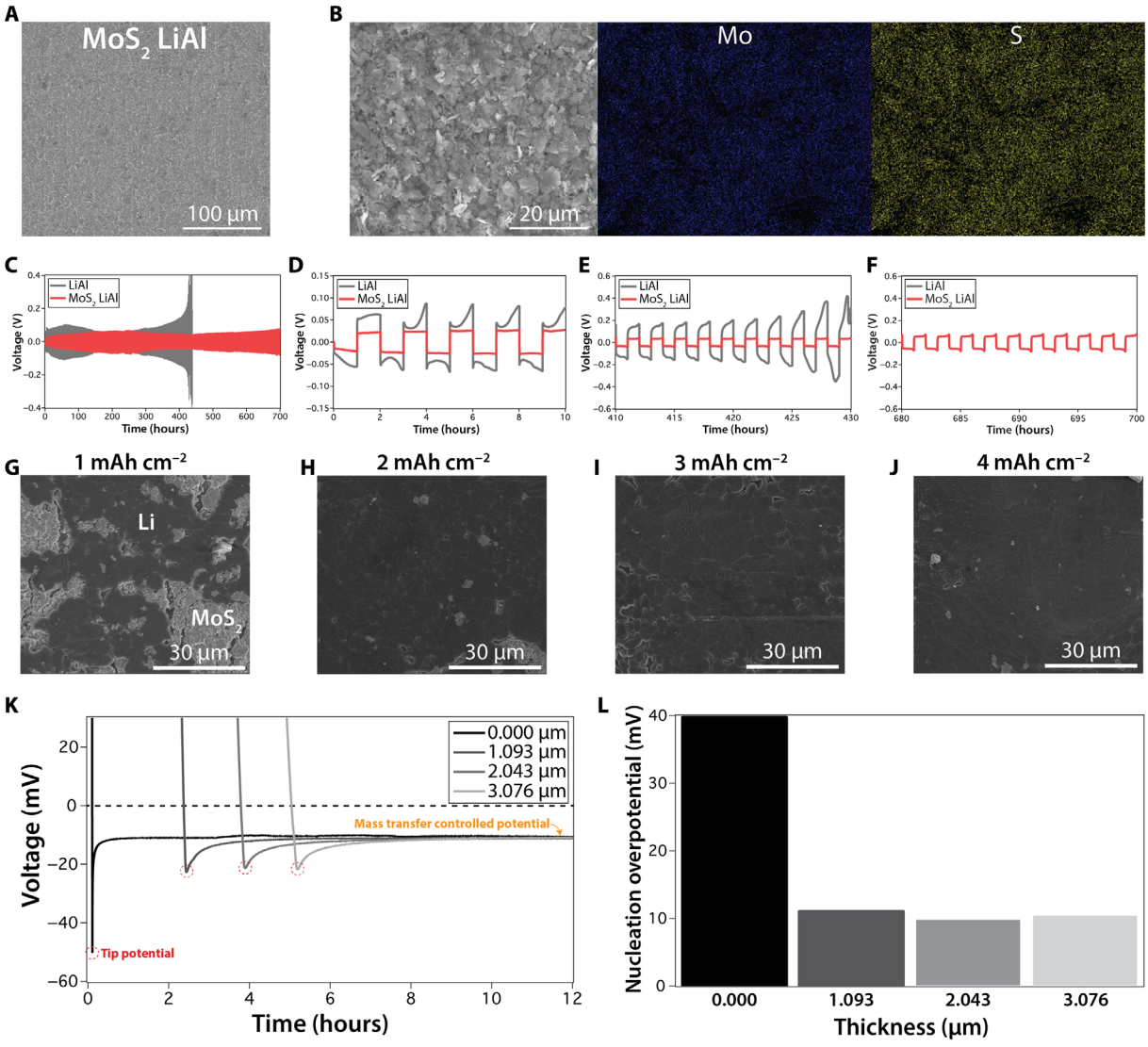


**Fig. 5. Electrochemical performances of the $MoS_2$ LiAl anode.** (**A**) Surface morphology of the uncycled $MoS_2$ LBASEI–coated LiAl ($MoS_2$ LiAl) anode. The SEM image exhibits uniform coating of the $MoS_2$ LiAl anode. (**B**) SEM image of the $MoS_2$ LiAl anode (left) with EDX elemental mappings of Mo (middle) and S (right). (**C**) Galvanostatic Li migration voltage profiles of LiAl|LiAl and LiAl $MoS_2$|$MoS_2$ LiAl symmetric cells at a fixed current density of 1 mA $cm^{-2}$ and a capacity of 1 mAh $cm^{-2}$. Magnified Li migration voltage profiles of (C) from (**D**) 0 to 10 hours, from (**E**) 410 to 430 hours, and from (**F**) 780 to 800 hours. Surface morphologies of (**G**) 1 mAh $cm^{-2}$, (**H**) 2 mAh $cm^{-2}$, (**I**) 3 mAh $cm^{-2}$, and (**J**) 4 mAh $cm^{-2}$ Li deposited onto $MoS_2$ LiAl from a LiAl $MoS_2$|$MoS_2$ LiAl symmetric cell at a fixed current density of 1 mA $cm^{-2}$. (**K**) Galvanostatic Li deposition voltage profiles of Cu $MoS_2$|$MoS_2$ LiAl asymmetric cells based on $MoS_2$ LBASEI thicknesses measured at the fixed current density of 0.05 mA $cm^{-2}$. The nucleation overpotentials of $MoS_2$ LBASEI are measured by taking the differences between the tip potential and the mass transfer-controlled potential. The horizontal dashed line represents 0 V where the Li deposition, the overplating of Li on $MoS_2$ LBASEI, starts. (**L**) The Li nucleation overpotentials based on $MoS_2$ LBASEI thicknesses ranging from 0 to 3.076 μm from Cu $MoS_2$|$MoS_2$ LiAl asymmetric cells.

The results show that $MoS_2$ LBASEI not only stabilizes Li migration to the LiAl anode but also promotes compact deposition of Li over large areas of the anode.

Applications of the $MoS_2$ LiAl anodes in $MoS_2$ LiAl|NCM811 full cells would expose the anodes to much higher potentials than in the symmetric cells. Figure 6 (A to C) reports results from SEM analysis of charged $MoS_2$ LiAl anodes, where the images for the targeted area of the anode are shown in the inset. It is seen that Li tends to deposit primarily around the edges of the smallest features, presumably due to the biased electric field induced by the high surface energy at the edges. Hence, Li deposits are observed entirely from the edges to the center of the $MoS_2$ LiAl anode. Figure 6A shows the SEM image of the Li electrodeposits at the edge of the $MoS_2$ LiAl anode, and compact Li electrodeposits are observed. Figure 6B shows the SEM image of Li electrodeposits in between the edge and the center of the charged $MoS_2$ LiAl anode, which exhibits uniform electrodeposits of Li. The Li electrodeposits around the center of the charged $MoS_2$ LiAl anode, as shown in Fig. 6C, are scarcely covered; however, Li electrodeposits are still smooth and uniform. To further demonstrate smooth Li deposition around the center of the anode, a cross-sectional image of the electrodeposit Li on the cycled $MoS_2$ LiAl anode after charging from the full cell is shown in fig. S9D. The image reveals a compact and smooth deposition of Li on the cycled $MoS_2$ LiAl. Furthermore, the SEM images of both charged and discharged $MoS_2$ LiAl anodes are investigated.

Downloaded from http://advances.sciencemag.org/ on October 31, 2019

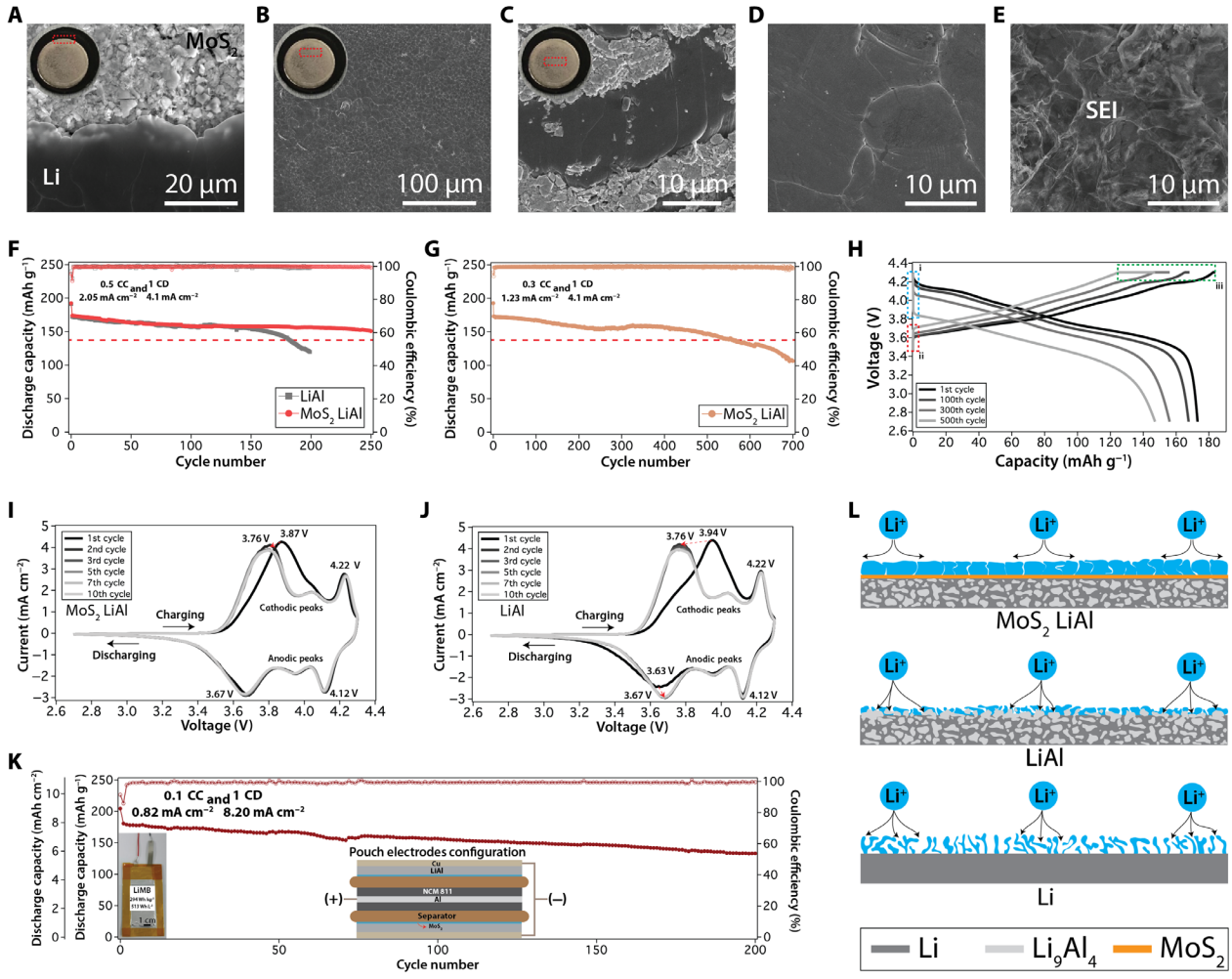


**Fig. 6. Investigating full-cell operations with the $MoS_2$ LiAl anode.** Morphologies of Li electrodeposits for the charged $MoS_2$ LiAl anode from the $MoS_2$ LiAl|NCM811 full cell taken (**A**) at the edge, (**B**) between the edge and the center, and (**C**) at the center of the charged $MoS_2$ LiAl anode. The charging C rate used is 0.5 CC. SEM images of (**D**) the charged $MoS_2$ LiAl anode and (**E**) the discharged $MoS_2$ LiAl anode, in which the electrodeposits of Li and the corresponding SEI are shown. (**F**) Cycling profiles based on the discharge capacities (filled symbols) and Coulombic efficiencies (open symbols) for LiAl|NCM811 and $MoS_2$ LiAl|NCM811 full cells at 0.5 CC and 1 CD with a voltage window of 2.7 to 4.3 V. (**G**) Cycling profiles based on the discharge capacities (filled symbols) and Coulombic efficiencies (open symbols) for the $MoS_2$ LiAl|NCM811 full cell at 0.3 CC and 1 CD with a voltage window of 2.7 to 4.3 V. (**H**) Corresponding voltage profiles of the $MoS_2$ LiAl|NCM811 full cell in (G) for the 1st to the 500th cycle. Region i represents the initial voltage profiles during the cell discharge. Region ii represents the initial voltage profiles during the cell charge. Region iii represents the voltage profiles at the constant voltage charging. Cyclic voltammograms of (**I**) $MoS_2$ LiAl|NCM811 and (**J**) LiAl|NCM811 full cells at a scan rate of 0.1 mV $s^{-1}$ with a voltage window of 2.7 to 4.3 V. (**K**) Cycling profiles based on the areal and gravimetric discharge capacities (filled symbols) and Coulombic efficiencies (open symbols) for the $MoS_2$ LiAl|NCM811 pouch cell at 0.1 CC and 1 CD with a voltage window of 2.7 to 4.3 V. The specifications for the pouch cell are 196 mAh, 294 Wh $kg^{-1}$, and 513 Wh $liter^{-1}$, and details are further provided in Materials and Methods. The insets represent the real image of and the stacking configuration used for the pouch cell. (**L**) Schematic illustration for and comparison of the Li migration process occurring at $MoS_2$ LiAl, LiAl, and Li anodes.

Figure 6D shows a closer look of Li electrodeposits of the charged $MoS_2$ LiAl, whereas Fig. 6E shows the discharged $MoS_2$ LiAl anode. As expected, very uniform and flat Li electrodeposits are observed, and the SEIs shown in Fig. 6E resemble the electrodeposited Li morphology in Fig. 6D from the previous stage, confirming the achievement of the stable Li migration processes in the full cell. These outcomes confirm that the smoother, less dendritic deposition of Li is achieved for the $MoS_2$ LiAl anode in the full cell, demonstrating stable and reversible redox processes.

Interfacial impedances and practical capacities of Li, LiAl, and $MoS_2$ LiAl electrodes are considered next. Nyquist plots for these electrodes are shown in fig. S10A, where it is seen that the impedance is lowest for $MoS_2$ LiAl and largest for Li, which comports with the initial Li migration voltage of Li (231 mV), LiAl (25.6 mV), and $MoS_2$ LiAl (13.8 mV). An essential operating criterion for LiMBs is the practical capacity ratio of the negative (anode) to the positive (cathode) electrode, termed the n/p ratio. To calculate the n/p ratio, the measured practical capacities of $MoS_2$ LiAl, LiAl, and Li anodes are shown in fig. S10B, which are 32.46 mAh $cm^{-2}$/3215.28 mAh $g^{-1}$, 34.49 mAh $cm^{-2}$/3215.28 mAh $g^{-1}$, and 39.83 mAh $cm^{-2}$/3723.57 mAh $g^{-1}$, respectively. These values are 80.42, 83.49, and 96.55% of the theoretical capacities of the LiM anode, corresponding to the same thickness. Note that the percentages of the theoretical capacities are based on the average of the theoretical gravimetric and areal capacities. In comparison, the

Downloaded from http://advances.sciencemag.org/ on October 31, 2019

theoretical capacity of the 200-μm Li foil is 41.22 mAh $cm^{-2}$. These also evidently follow the expected trend as the LiM anode has the largest capacity and LiAl and $MoS_2$ LiAl electrodes have lesser capacities owing to compensation of active Li for the formation of the $Li_9Al_4$ intermetallic compound in the LiAl anode as well as for the lithiation and SEI formation of the $MoS_2$ LBASEI.

To systematically analyze the practical capacity of LiAl, the 80 wt % Li and 20 wt % Al mixture LiAl alloy yields 73 wt % Li and 27 wt % $Li_9Al_4$ using the Lever rule in the phase diagram as shown in fig. S1A, and multiplying the 73 wt % of Li with the LiM anode capacity yields about 10% deviation from the theoretical capacity to the experimental capacity. As the practical cathode capacity of 4.1 mAh $cm^{-2}$ at 0.1 CD is used to construct the full cells, the corresponding n/p ratios for the full cell using the $MoS_2$ LiAl, LiAl, and Li anodes are 7.9, 8.4, and 9.7, respectively, where these numbers represent the excess amount of practically active Li with respect to the practical capacity of the cathode. The cycle life of cells using these anodes varies in the opposite order: $MoS_2$ LiAl (250 cycles) > LiAl (180 cycles) > Li (73 cycles) at 0.5 CC (2.05 mA $cm^{-2}$) and 1 CD (4.1 mA $cm^{-2}$). Here, the cycle life is defined as the number of charge-discharge cycles where the cell maintains at least 80% of its initial capacity, as illustrated in Figs. 6F and 3L. Figure 6L illustrates, in schematic form, our proposed mechanism through which $MoS_2$ LiAl and LiAl achieve improved reversibility relative to Li anodes. The evolution in the morphology of the SEIs of the cycled $MoS_2$ LiAl, LiAl, and Li anodes is shown in fig. S11—from irregular and porous for Li (fig. S11A) to more compact for LiAl (fig. S11B) and, last, to uniform and flat for $MoS_2$ LiAl (fig. S11C). Direct observation of these SEIs demonstrates stabilizing Li migration processes, which agree with the abovementioned computational and experimental results.

As the cycling performance and the reversibility of the cells are restricted by the high interfacial impedance of the anode, lowering the charging C rate would slow down the rate of impedance buildup, thus enhancing cycle life. To evaluate this, the cycling behavior of $MoS_2$ LiAl|NCM811 full cells is investigated at different charging C rates, 0.5 CC and 0.3 CC, with the same discharge C rate of 1 CD. In Fig. 6F, cycling performances of LiAl and $MoS_2$ LiAl full cells are shown with 0.5 CC and 1 CD. Under these cycling C rates, the full cell with the $MoS_2$ LiAl anode cycles more than 250 cycles, whereas the full cell with LiAl fails under 180 cycles. Cycling $MoS_2$ LiAl|NCM811 full cells at a charging C rate of 0.3 CC corresponding to a current density of 1.23 mA $cm^{-2}$, as shown in Fig. 6G, yields more than twice (from 250 to >550 cycles) the cycle life. Figure 6H reports the corresponding voltage profiles for the 1st, 100th, 300th, and 500th cycles. The profiles exhibit steep changes (regions i and ii) and longer constant voltage charging tails (region iii) as cycle number increases. The voltage profile evolutions are consistent with electrochemical performance degradation due to impedance buildup at the anode. This conclusion is made more concrete using CV to interrogate the redox reactions during charging and discharging processes in LiM full cells using $MoS_2$ LiAl (Fig. 6I) and LiAl (Fig. 6J) as anodes. Figure 6I shows that the position and amplitude of the redox peaks are unchanged during repeated anodic and cathodic sweeps. Also, between the very first and the second cathodic sweeps, there is a voltage shift due to the activation of the cell, and the voltage shifts from high to low as indicated by the red arrow in Fig. 6I. The voltage magnitude of the cathodic peak change from the first to the second cycle is 110 mV. Also, the voltage difference between the redox peaks involving $Ni^{2+}$, $Ni^{3+}$, and $Ni^{4+}$ at the first cycle is 200 mV. As a comparison, the cyclic voltammograms for LiAl|NCM811 full cells are shown in Fig. 6J. The voltage magnitude of the cathodic peak change from the first to the second cycle is 180 mV. Also, the voltage difference between the redox peaks involving $Ni^{2+}$, $Ni^{3+}$, and $Ni^{4+}$ at the first cycle is 310 mV. Thus, greater cathodic peak shifts and redox peaks are observed from the first to the second cathodic and anodic sweeps compared to the results for $MoS_2$ LiAl|NCM811 cells, and the results are in agreement with the impedance trend reported in fig. S10A. Despite the bigger voltage shifts, however, the redox peaks remain steady under repeated cathodic and anodic sweeps, supporting the conclusion that it is the interphases, not the reversibility of the electrochemical reactions at the LiAl anode, that are responsible for the reduced cycle life. The CV measurements also confirm that $MoS_2$ LBASEI does not contribute appreciably to the electrode redox reactions, as no additional redox peaks are observed. Furthermore, the results show that the $Li_9Al_4$ intermetallic compound acts essentially as a host for Li deposition as no new redox peaks are seen, relative to what is observed in Li|NCM811 full cells (*49*). Further efforts were invested to demonstrate our findings in the larger-format LiMB pouch cell (196 mAh, 294 Wh $kg^{-1}$, and 513 Wh $liter^{-1}$) using $MoS_2$ LiAl anodes and NCM811 cathodes. The electrochemical cycling characteristics of these cells are reported in Fig. 6K; the subsets represent the actual image and the stacking configuration of the constructed LiMB. The results reported in Fig. 6K show that stable cycling is achieved for more than 200 cycles with practical parameter values such as a cathode capacity of 4.1 mAh $cm^{-2}$, an n/p ratio of 7.9, and an electrolyte amount of 2.03 μl $mAh^{-1}$, consistent with the improved reversibility evident from our coin cell studies reported in the previous sections.

In conclusion, by combining detailed computational studies of electrode structures, Li adatom binding, and transport in model Li and $Li_9Al_4$ intermetallic anode systems in a vacuum environment with experimental studies of Li electrodeposition on anodes in liquid electrolytes, we investigate how the electrode structure, adatom binding, and surface diffusion of Li influence the stability of the anodes. In addition, through theoretical and empirical analyses of these processes on electrodes protected by well-defined $MoS_2$ LBASEI, we study the effect of interface structure and transport on long-term stability in LiMBs. Our findings are used to develop advanced LiMB anodes with well-formed SEIs to facilitate uniform Li migration. It is shown that these efforts yield significant improvements in the magnitude and stability of interfacial impedance of the anode and extends the cycle life of full-cell batteries in which the anodes are paired with commercial intercalating NCM811 cathodes. Building on these observations, we create larger-format pouch cell batteries with practical parameters and energy densities and show that they exhibit impressive stability in electrochemical cycling. While further engineering efforts are required to construct reliable LiMBs with lower n/p ratios and electrode volume and larger cell capacities that use the findings reported herein, our studies provide a robust foundation of knowledge upon which to build such efforts.

## MATERIALS AND METHODS

### Fabrication of LiAl alloy

A LiAl ingot was used to fabricate LiAl foil with a uniform thickness of 200 μm. A 300-g LiAl ingot composed of 80 wt % high-purity Li (99.99%) and 20 wt % granular Al powder (φ 2 to 3 μm) was formed by direct mixing of the components at 230 to 250°C for 30 to 35 min under an Ar atmosphere. After fine mixing, the ingot was cooled to room temperature and subsequently roll-pressed to obtain 30 m of 200-μm-thick LiAl foil. The roll-press process was also carried out in an inert Ar-filled atmosphere at the Honjo Metal facility in Japan and supplied by Honjo Metal Japan through The Kyung-In Synthetic Company

Downloaded from http://advances.sciencemag.org/ on October 31, 2019

(KISCO) Korea. The obtained LiAl foil was cut into circular disks (φ 15 mm) for the electrochemical measurements discussed in the following sections.

### First-principles structure and transport calculations for Li, $Li_9Al_4$, and $MoS_2$

The first-principles calculations were performed within the framework of DFT, as implemented in the Vienna ab initio simulation package (VASP.5.3.2). The electronic exchange-correlation interactions were incorporated using generalized gradient approximation proposed by Perdew, Burke, and Ernzerhof, and electron-ion interaction using projected augmented wave formalism. The electronic wave function was described using plane-wave basis set as a linear combination of the single-particle Kohn-Sham orbitals for periodic systems. To control the number of plane waves, the energy cutoff of 500 eV was used. For *k*-space sampling of the first Brillouin zone, Monkhorst *k*-space mesh of 3 by 3 by 1 was used for periodic systems. A vacuum layer of 20 Å was included above the surface layer of atoms to minimize the interlayer interactions along the nonperiodic direction of the supercells. All the atoms were relaxed, and the force on each atom was <0.01 eV $Å^{-1}$.

To study the Li interactions on the LiAl surface, the bulk unit cell with two molecules of the $Li_9Al_4$ (Fig. 4G) was used to construct the 2 by 2 by 1 supercell slab model for the $Li_9Al_4$ (−121) surface. However, for the Li interactions on the Li surface, a 4 by 4 by 1 supercell was used to construct the slab model for the Li (110) surface. To generate the surface layer of $Li_9Al_4$ (−121) and Li (110), the slab model was constructed followed by a vacuum layer of 20 Å. To understand the clustering of Li on $Li_9Al_4$ and Li surfaces, optimization of isolated Li clusters was performed under the *k*-space of 1 by 1 by 1 in a cubic cell of 20-Å dimension. To incorporate $MoS_2$ LBASEI, a 4 by 4 by 1 supercell was considered for the two phases of $MoS_2$, known as $MoS_2$ 2H and $MoS_2$ T. Helmholtz free-energy analysis was performed on both the phases of $MoS_2$ to understand the in situ phase transformation of the $MoS_2$. The electronic band structure of $MoS_2$ 2H and $MoS_2$ T was calculated to interpret the semiconducting and metallic characteristics of the 2H and T phase of $MoS_2$, respectively. The lithiation process of $MoS_2$ was performed by adsorbing the Li atoms successively one after the other on both sides of the $MoS_2$ T.

The binding energy of Li adsorbed on the surface is defined as

$$E = E_{\text{total}} - [E_{\text{Li}} + E_{\text{surface}}]$$

where $E_{\text{total}}$, $E_{\text{Li}}$, and $E_{\text{surface}}$ are the total energy of the surface after the Li adsorption, the energy of a single Li atom, and the energy of the surface before Li adsorption, respectively. As per the binding energy expression, the negative value of the binding energy infers the stable bound state of the system.

To study Li migration behavior on Li, $Li_9Al_4$, and $MoS_2$ surfaces, the CI-NEB method (*41*) analysis was performed. CI-NEB further helped to determine the minimum energy migration path of Li over Li, $Li_9Al_4$, and $MoS_2$ surfaces. The activation energy was determined using the energy barrier height of the minimum energy path followed by the migrating Li on the surface. The value of activation energy corresponds to the threshold energy required by Li atom to migrate from the first minimum energy state to the adjacent minimum energy state.

### Fabrication of $MoS_2$ LBASEI

$MoS_2$ LBASEI was fabricated by performing the LBS process. To perform LBS for $MoS_2$, a $MoS_2$ suspension was firstly made by mixing 5 wt % of $MoS_2$ particles (Sigma-Aldrich, <2 μm, 99%) in pure ethanol. The $MoS_2$ suspension was sonicated for 20 min to evenly disperse the particles in ethanol. With this suspension, LBS was used to create the LBASEI on Cu foil. The 6 cm by 10 cm Cu foil was used as the coating substrate and submerged into a water-filled container, and the $MoS_2$ suspension was injected at the surface of the water to coat $MoS_2$ LBASEI on Cu substrate. This process was conducted until the desired thickness of $MoS_2$ LBASEI was obtained. After obtaining the $MoS_2$ LBASEI–coated Cu, the sample was dried on a hot plate at 100°C for 1 min first and then it was transferred to a vacuum oven to dry overnight at 50°C. The thickness of $MoS_2$ LBASEI was measured by a LEXT OLS4100 microscope (Olympus) using a 3D-mapping tool. All of these processes were conducted under ambient conditions, and the coating thickness of $MoS_2$ LBASEI ranged from 1.093 to 3.076 μm.

### Fabrication of $MoS_2$ LiAl electrodes

$MoS_2$ LBASEI–coated LiAl ($MoS_2$ LiAl) electrodes were fabricated by transferring $MoS_2$ LBASEI on Cu to 4 cm by 5 cm LiAl foil via the roll-press process. Under dry atmosphere at a dew point below −70°C, the configuration of Mylar-film|Cu|$MoS_2$ LBASEI|LiAl|Cu|Mylar-film was used for the roll-press process, and the stacked components were uniformly pressed with a cylinder distance of 70 to 80% of the total thickness of the stacked components and with a rolling rate of 0.5 cm $s^{-1}$, and after the press, Mylar films and Cu of $MoS_2$ LBASEI were detached to make a final transfer of $MoS_2$ LBASEI to the LiAl foil. $MoS_2$ LiAl was cut into circular disks (φ 15 mm) to fabricate coin cells for electrochemical measurements.

### Characterization and electrochemical analysis of the electrodes

The crystal structure of LiAl was characterized by XRD patterns (D/MAC, Inspect F50, Rigaku). To prepare the XRD samples of LiAl, LiAl was covered with Kapton tape under dry atmosphere below the dew point of −70°C to protect the sample, where the XRD measurements were conducted under atmospheric conditions. The surface morphologies of the samples were investigated via SEM by Teneo Volume Scope SEM and FIB microscopy by Quanta 3D FEG FEI. The cycled samples for the microscopy measurements were cleaned and washed with dimethyl carbonate (DMC) solvent and dried overnight in a vacuum of at 50°C and were transferred to a vacuum chamber for surface analysis via SEM and FIB. Accelerating voltages of 5 and 14 kV were used for SE mode and BSE mode to observe the surfaces of the samples. For the FIB milling of the samples, the accelerating voltage of 30 kV and beam currents of 7 nA (rough milling) and 0.5 nA (fine milling) were used to observe the surface of the samples.

For the electrochemical measurements, 2032 coin cell parts of the cases, gasket, and 1-mm spacer by Wellcos Japan were used to construct coin cells. The electrolyte composed of 0.6 M lithium bis(trifluoromethanesulfonyl) imide (LiTFSI; 99.95%, Sigma-Aldrich), 0.4 M lithium bis-(oxalato) borate (LiBOB; Sigma-Aldrich), 0.4 M lithium fluoride (LiF; 99.99%, Sigma-Aldrich), 0.1 M lithium nitrate ($LiNO_3$; 99.99%, Sigma-Aldrich), 0.05 M lithium hexafluorophosphate ($LiPF_6$; PanaX Etech), 0.03 M lithium tetrafluoroborate ($LiBF_4$; 99.99%, Sigma-Aldrich) dissolved in ethylene carbonate (EC; PanaX Etech):DMC (PanaX Etech) by a 1:1 volume ratio with 1 wt % fluoroethylene carbonate (FEC; PanaX Etech), and 3 wt % di-2,2,2-trifluoroethyl carbonate (TFEC, TCI Tokyo Chemical) was used for the electrochemical measurements. For the electrolyte synthesis, the salts were dissolved into the EC:DMC solvent first by stirring for 48 hours followed by 5-min sonication

Downloaded from http://advances.sciencemag.org/ on October 31, 2019

under inert conditions, and FEC and TFEC additives were included afterward.

For the Li stripping and plating measurements, Li|Li, LiAl|LiAl, and LiAl $MoS_2$|$MoS_2$ LiAl symmetric cells were used to obtain voltage profiles under a current density of 1 mA $cm^{-2}$ and a capacity of 1 mAh $cm^{-2}$. The disk size of φ 15 mm was used for the electrodes of all the symmetric cells, and an 11-μm polyethylene (PE) separator (W-Scope Korea) with a disk size of φ 18 mm was used. Thirty microliters of the electrolyte was used to construct the symmetric cells. The measurements were performed using the battery cycler (Maccor Series 4000).

An asymmetric coin cell was used to measure the nucleation overpotentials of $MoS_2$ LBASEI. The electrode configuration is Cu $MoS_2$|$MoS_2$ LiAl, where the thickness of $MoS_2$ ranged from 1.093 to 3.076 μm for the nucleation overpotential measurements. A disk size of φ 16 mm was used for the Cu $MoS_2$, and a disk size of φ 15 mm was used for $MoS_2$ LiAl. The 11-μm-thick PE separator and 30 μl of the electrolyte were used to construct asymmetric cells for the measurement. A galvanostatic potentiostat (Biologics VSP/VMP3) was used to measure the nucleation overpotential with the procedure of applying a current density of 0.05 mA $cm^{-2}$ for the desired amount of time.

For the full cell measurements, the cathode of 4.1 mAh $cm^{-2}$ NCM811 (LG Chem) with a disk size of φ 12 mm and the anode of 200-μm-thick Li, 200-μm-thick LiAl, and 202-μm-thick $MoS_2$ LiAl with a disk size of φ 15 mm were used as the electrodes. The 11-μm-thick PE separator with a disk size of φ 18 mm and 30 μl of the electrolyte (7.3 μl $mAh^{-1}$) were used to construct the full cells for the cycling measurements. All of the full cells were fabricated under dry atmosphere with a dew point below −70°C. The charging steps were divided into two parts: galvanostatic charging and constant voltage charging. The full cells were charged up to 4.3 V under the galvanostatic condition followed by the constant voltage charging with a cutoff current value of 0.05 C. For the discharge process, the galvanostatic current was applied for the discharging process until the voltage reached 2.7 V. Two charging C rates, 0.5 CC and 0.3 CC, and the single discharge C rate, 1 CD, were used to measure the full cell with a voltage window of 2.7 to 4.3 V. One formation cycle is performed at 0.1 CC and 0.1 CD. The Maccor battery cycler was used to measure cycling performances.

For the pouch cell, the configuration of 8-μm Cu|202-μm $MoS_2$ LiAl|68-μm NCM811|12-μm Al|68-μm NCM811|202-μm $MoS_2$ LiAl|8-μm Cu was used to construct 196-mAh LiMB. Two 4 cm by 6 cm $MoS_2$ LiAl anodes, a single 4 cm by 6 cm double-sided cathode, two 5 cm by 7 cm PE separators, and 400 μl of the electrolyte and 200 μl for each anode/cathode interface were used. To calculate the gravimetric and volumetric energy densities of the pouch cell, the following parameters were used: Al (thickness, 12 μm; areal weight, 3.24 mg $cm^{-2}$), NCM811 (areal capacity, 4.1 mAh $cm^{-2}$; thickness, 68 μm; areal weight, 22.48 mg $cm^{-2}$), Cu (thickness, 8 μm; areal weight, 7.168 mg $cm^{-2}$), $MoS_2$ LiAl (thickness, 202.04 μm; areal capacity, 32.46 mAh $cm^{-2}$; areal weight, 13.01 mg $cm^{-2}$), PE separator (thickness, 11 μm; areal weight, 0.45 mg $cm^{-2}$), electrolyte (amount, 400 μl; density, 1.17 mg $\mu l^{-1}$; normalized amount, 2.03 μl $mAh^{-1}$), and a reaction potential of 3.8 V. The gravimetric and volumetric energy densities of the pouch cell were 294 Wh $kg^{-1}$ and 513 Wh $liter^{-1}$, respectively. All of the battery components were prepared under dry atmosphere with a dew point below −70°C. The charging steps were divided into two parts: galvanostatic charging and constant voltage charging. The pouch battery was charged up to 4.3 V under galvanostatic conditions followed by the constant voltage charging with a cutoff current value of 0.05 C. For the discharge process, the galvanostatic condition was applied for the discharging process until the voltage reached 2.7 V. The charging C rates of 0.1 CC and discharging C rate of 1 CD were used to measure the pouch battery with a voltage window of 2.7 to 4.3 V. One formation cycle was performed at 0.1 CC and 0.1 CD. The Maccor battery cycler was used to measure the electrochemical cycling performance.

The cyclic voltammograms and Nyquist plots were measured by the potentiostat (Biologics VSP/VMP3). For the CV, the full cells were scanned with a voltage window of 2.7 to 4.3 V and a scan rate of 0.1 mV $s^{-1}$. For Nyquist plots, AC impedance measurements were performed for the symmetric cells with a frequency range of 1 MHz to 0.5 Hz.

## SUPPLEMENTARY MATERIALS

Supplementary material for this article is available at http://advances.sciencemag.org/cgi/content/full/5/10/eaax5587/DC1

Fig. S1. LiAl phase diagram and XRD patterns of the LiAl anode.
Fig. S2. SEM and FIB analysis of the LiAl anode.
Fig. S3. Li migration behavior of the Li (110) surface.
Fig. S4. SEM image of Li electrodeposits on the Li anode.
Fig. S5. AC impedance measurements for LiAl and Li anodes.
Fig. S6. SEM images of cycled LiAl and Li anodes from the full cell.
Fig. S7. Optical images of LiAl and $MoS_2$ LiAl anodes.
Fig. S8. Atomic structures of $MoS_2$ 2H and $MoS_2$ T.
Fig. S9. SEM images of Li electrodeposits on the $MoS_2$ LiAl anode.
Fig. S10. AC impedance and practical areal capacity measurements for Li, LiAl, and $MoS_2$ LiAl anodes.
Fig. S11. SEM images of SEI for Li, LiAl, and $MoS_2$ LiAl anodes.
Table S1. The binding energies of Li clusters on Li (110) and $Li_9Al_4$ (−121) surfaces.

## REFERENCES AND NOTES


1. P. Albertus, S. Babinec, S. Litzelman, A. Newman, Status and challenges in enabling the lithium metal electrode for high-energy and low-cost rechargeable batteries. *Nat. Energy* **3**, 16–21 (2018).
2. M. Winter, B. Barnett, K. Xu, Before Li ion batteries. *Chem. Rev.* **118**, 11433–11456 (2018).
3. J. Liu, Z. Bao, Y. Cui, E. J. Dufek, J. B. Goodenough, P. Khalifah, Q. Li, B. Y. Liaw, P. Liu, A. Manthiram, Y. S. Meng, V. R. Subramanian, M. F. Toney, V. V. Viswanathan, M. S. Whittingham, J. Xiao, W. Xu, J. Yang, X.-Q. Yang, J.-G. Zhang, Pathways for practical high-energy long-cycling lithium metal batteries. *Nat. Energy* **4**, 180–186 (2019).
4. D. Lin, Y. Liu, Y. Cui, Reviving the lithium metal anode for high-energy batteries. *Nat. Nanotechnol.* **12**, 194–206 (2017).
5. S. Jiao, X. Ren, R. Cao, M. H. Engelhard, Y. Liu, D. Hu, D. Mei, J. Zheng, W. Zhao, Q. Li, N. Liu, B. D. Adams, C. Ma, J. Liu, J.-G. Zhang, W. Xu, Stable cycling of high-voltage lithium metal batteries in ether electrolytes. *Nat. Energy* **3**, 739–746 (2018).
6. S. Wei, Z. Cheng, P. Nath, M. D. Tikekar, G. Li, L. A. Archer, Stabilizing electrochemical interfaces in viscoelastic liquid electrolytes. *Sci. Adv.* **4**, eaao6243 (2018).
7. Z. Zeng, V. Murugesan, K. S. Han, X. Jiang, Y. Cao, L. Xiao, X. Ai, H. Yang, J.-G. Zhang, M. L. Sushko, J. Liu, Non-flammable electrolytes with high salt-to-solvent ratios for Li-ion and Li-metal batteries. *Nat. Energy* **3**, 674–681 (2018).
8. Q. Pang, A. Shyamsunder, B. Narayanan, C. Y. Kwok, L. A. Curtiss, L. F. Nazar, Tuning the electrolyte network structure to invoke quasi-solid state sulfur conversion and suppress lithium dendrite formation in Li–S batteries. *Nat. Energy* **3**, 783–791 (2018).
9. M. J. Zachman, Z. Tu, S. Choudhury, L. A. Archer, L. F. Kourkoutis, Cryo-STEM mapping of solid–liquid interfaces and dendrites in lithium-metal batteries. *Nature* **560**, 345–349 (2018).
10. X. Fan, L. Chen, O. Borodin, X. Ji, J. Chen, S. Hou, T. Deng, J. Zheng, C. Yang, S.-C. Liou, K. Amine, K. Xu, C. Wang, Non-flammable electrolyte enables Li-metal batteries with aggressive cathode chemistries. *Nat. Nanotechnol.* **13**, 715–722 (2018).
11. M. S. Kim, J.-H. Ryu, Deepika, Y. R. Lim, I. W. Nah, K.-R. Lee, L. A. Archer, W. I. Cho, Langmuir–Blodgett artificial solid-electrolyte interphases for practical lithium metal batteries. *Nat. Energy* **3**, 889–898 (2018).
12. M. D. Tikekar, L. A. Archer, D. L. Koch, Stabilizing electrodeposition in elastic solid electrolytes containing immobilized anions. *Sci. Adv.* **2**, 1600320 (2016).
13. M. D. Tikekar, S. Choudhury, Z. Tu, L. A. Archer, Design principles for electrolytes and interfaces for stable lithium-metal batteries. *Nat. Energy* **1**, 16114 (2016).
14. J. Qian, B. D. Adams, J. Zheng, W. Xu, W. A. Henderson, J. Wang, M. E. Bowden, S. Xu, J. Hu, J.-G. Zhang, Anode-free rechargeable lithium metal batteries. *Adv. Funct. Mater.* **26**, 7094–7102 (2016).


Downloaded from http://advances.sciencemag.org/ on October 31, 2019

15. H. Ota, K. Shima, M. Ue, J.-i. Yamaki, Effect of vinylene carbonate as additive to electrolyte for lithium metal anode. *Electrochim. Acta* **49**, 565–572 (2004).
16. X. Yin, W. Tang, I. D. Jung, K. C. Phua, S. Adams, S. W. Lee, G. W. Zheng, Insights into morphological evolution and cycling behaviour of lithium metal anode under mechanical pressure. *Nano Energy* **50**, 659–664 (2018).
17. H. Chen, A. Pei, D. Lin, J. Xie, A. Yang, J. Xu, K. Lin, J. Wang, H. Wang, F. Shi, D. Boyle, Y. Cui, Uniform high ionic conducting lithium sulfide protection layer for stable lithium metal anode. *Adv. Energy Mater.* **9**, 1900858 (2019).
18. Q. Zhao, X. Liu, S. Stalin, K. Khan, L. A. Archer, Solid-state polymer electrolytes with in-built fast interfacial transport for secondary lithium batteries. *Nat. Energy* **4**, 365–373 (2019).
19. X. Shen, Y. Li, T. Qian, J. Liu, J. Zhou, C. Yan, J. B. Goodenough, Lithium anode stable in air for low-cost fabrication of a dendrite-free lithium battery. *Nat. Commun.* **10**, 900 (2019).
20. Q. Liu, S. Zhou, C. Tang, Q. Zhai, X. Zhang, R. Wang, Li-B alloy as an anode material for stable and long life lithium metal batteries. *Energies* **11**, 2512 (2018).
21. L.-L. Kong, L. Wang, Z.-C. Ni, S. Liu, G.-R. Li, X.-P. Gao, Lithium–magnesium alloy as a stable anode for lithium–sulfur battery. *Adv. Funct. Mater.* **29**, 1808756 (2019).
22. B. Sun, J. Lang, K. Liu, N. Hussain, M. Fang, H. Wu, Promoting a highly stable lithium metal anode by superficial alloying with an ultrathin indium sheet. *Chem. Commun.* **55**, 1592–1595 (2019).
23. Z. Tu, S. Choudhury, M. J. Zachman, S. Wei, K. Zhang, L. F. Kourkoutis, L. A. Archer, Fast ion transport at solid–solid interfaces in hybrid battery anodes. *Nat. Energy* **3**, 310–316 (2018).
24. S. Choudhury, Z. Tu, S. Stalin, D. Vu, K. Fawole, D. Gunceler, R. Sundararaman, L. A. Archer, Electroless formation of hybrid lithium anodes for fast interfacial ion transport. *Angew. Chem. Int. Ed.* **56**, 13070–13077 (2017).
25. X. Liang, Q. Pang, I. R. Kochetkov, M. S. Sempere, H. Huang, X. Sun, L. F. Nazar, A facile surface chemistry route to a stabilized lithium metal anode. *Nat. Energy* **2**, 17119 (2017).
26. K. Yan, Z. Lu, H.-W. Lee, F. Xiong, P.-C. Hsu, Y. Li, J. Zhao, S. Chu, Y. Cui, Selective deposition and stable encapsulation of lithium through heterogeneous seeded growth. *Nat. Energy* **1**, 16010 (2016).
27. M. S. Kim, M.-S. Kim, V. Do, Y. R. Lim, I. W. Nah, L. A. Archer, W. I. Cho, Designing solid-electrolyte interphases for lithium sulfur electrodes using ionic shields. *Nano Energy* **41**, 573–582 (2017).
28. Z. Tu, S. Choudhury, M. J. Zachman, S. Wei, K. Zhang, L. F. Kourkoutis, L. A. Archer, Designing artificial solid-electrolyte interphases for single-ion and high-efficiency transport in batteries. *Joule* **1**, 394–406 (2017).
29. M. S. Kim, L. Ma, S. Choudhury, S. S. Moganty, S. Wei, L. A. Archer, Fabricating multifunctional nanoparticle membranes by a fast layer-by-layer Langmuir–Blodgett process: Application in lithium–sulfur batteries. *J. Mater. Chem. A* **4**, 14709–14719 (2016).
30. M. S. Kim, L. Ma, S. Choudhury, L. A. Archer, Multifunctional separator coatings for high-performance lithium–sulfur batteries. *Adv. Mater. Interfaces* **3**, 1600450 (2016).
31. M. N. Obrovac, V. L. Chevrier, Alloy negative electrodes for Li-ion batteries. *Chem. Rev.* **114**, 11444–11502 (2014).
32. B. M. L. Rao, R. W. Francis, H. A. Christopher, Lithium-aluminum electrode. *J. Electrochem. Soc.* **124**, 1490–1492 (1977).
33. A. N. Dey, Electrochemical alloying of lithium in organic electrolytes. *J. Electrochem. Soc.* **118**, 1547–1549 (1971).
34. T. O. Brun, J. D. Jorgensen, M. Misawa, F. J. Rotella, S. Susman, D. F. R. Mildner, Defects and disorder in the fast-ion electrode lithium-aluminum. *J. Electrochem. Soc.* **129**, 2509–2512 (1982).
35. T. R. Jow, C. C. Liang, Lithium-aluminum electrodes at ambient temperatures. *J. Electrochem. Soc.* **129**, 1429–1434 (1982).
36. A. S. Baranski, W. R. Fawcett, The formation of lithium-aluminum alloys at an aluminum electrode in propylene carbonate. *J. Electrochem. Soc.* **129**, 901–907 (1982).
37. W.-J. Zhang, Lithium insertion/extraction mechanism in alloy anodes for lithium-ion batteries. *J. Power Sources* **196**, 877–885 (2011).
38. J. Zhang, D. Y. W. Yu, Phase-pure P2-$Na_{0.7(1-x)}[Li_xMn_{1-x}]O_\delta$ as a cathode material for Na-ion batteries. *ChemElectroChem* **4**, 1287–1294 (2017).
39. X. Chen, X.-R. Chen, T.-Z. Hou, B.-Q. Li, X.-B. Cheng, R. Zhang, Q. Zhang, Lithiophilicity chemistry of heteroatom-doped carbon to guide uniform lithium nucleation in lithium metal anodes. *Sci. Adv.* **5**, eaau7728 (2019).
40. X. Fan, W. T. Zheng, J.-L. Kuo, D. J. Singh, Adsorption of single Li and the formation of small Li clusters on graphene for the anode of lithium-ion batteries. *ACS Appl. Mater. Interfaces* **5**, 7793–7797 (2013).
41. G. Henkelman, B. P. Uberuaga, H. Jónsson, A climbing image nudged elastic band method for finding saddle points and minimum energy paths. *J. Chem. Phys.* **113**, 9901–9904 (2000).
42. M. Jäckle, K. Helmbrecht, M. Smits, D. Stottmeister, A. Groß, Self-diffusion barriers: Possible descriptors for dendrite growth in batteries? *Energ. Environ. Sci.* **11**, 3400–3407 (2018).
43. S. Choudhury, S. Wei, Y. Ozhabes, D. Gunceler, M. J. Zachman, Z. Tu, J. H. Shin, P. Nath, A. Agrawal, L. F. Kourkoutis, T. A. Arias, L. A. Archer, Designing solid-liquid interphases for sodium batteries. *Nat. Commun.* **8**, 898 (2017).
44. E. Cha, M. D. Patel, J. Park, J. Hwang, V. Prasad, K. Cho, W. Choi, 2D $MoS_2$ as an efficient protective layer for lithium metal anodes in high-performance Li–S batteries. *Nat. Nanotechnol.* **13**, 337–344 (2018).
45. D. Nasr Esfahani, O. Leenaerts, H. Sahin, B. Partoens, F. M. Peeters, Structural transitions in monolayer $MoS_2$ by lithium adsorption. *J. Phys. Chem. C* **119**, 10602–10609 (2015).
46. X. Sun, Z. Wang, Y. Q. Fu, Defect-mediated lithium adsorption and diffusion on monolayer molybdenum disulfide. *Sci. Rep.* **5**, 18712 (2015).
47. B. Xu, L. Wang, H. J. Chen, J. Zhao, G. Liu, M. S. Wu, Adsorption and diffusion of lithium on 1T-$MoS_2$ monolayer. *Comput. Mater. Sci.* **93**, 86–90 (2014).
48. F. Holtstiege, P. Bärmann, R. Nölle, M. Winter, T. Placke, Pre-lithiation strategies for rechargeable energy storage technologies: Concepts, promises and challenges. *Batteries* **4**, 1–39 (2018).
49. J.-I. Lee, M. Shin, D. Hong, S. Park, Efficient Li-ion-conductive layer for the realization of highly stable high-voltage and high-capacity lithium metal batteries. *Adv. Energy Mater.* **9**, 1803722 (2019).


**Acknowledgments:** We acknowledge M.-H. Kim, H. Lee, and H. J. Hah at LG Chem Battery R&D for supplying the NCM811 cathode for this work. We also thank B.-H. Kim at the Platform Technology Laboratory, Korea Institute of Energy Research, and S. Boateng at the Computational Science Research Center, Korea Institute of Science and Technology, and Korea University of Science and Technology, for the useful discussions on the screening of Li adsorption sites for the LiAl intermetallic compound, and B.-H. Kim at W-Scope Korea for supplying the separator. D. and K.-R.L. thank Virtual Lab (www.virtuallab.co.kr) for the Cloud Computing Interface and KIST supercomputing facility. **Funding:** This work was supported by the National Research Foundation of Korea (NRF-2016M1B3A1A01937324 and NRF-2016M3A7B4025402), the Korea Institute of Science and Technology Institutional Program (project no., 2E29650), and the U.S. Advanced Research Projects Agency—Energy (ARPA-E) through award #DE-AR0000750. **Author contributions:** M.S.K., L.A.A., and W.I.C. designed and conceptualized the overall study. D. performed the first-principles calculations to investigate Li migrations for LiAl and $MoS_2$ species. S.H.L., M.-S.K., and J.-H.R. prepared $MoS_2$ LBASEI for the LiAl anode and provided technical support. K.-R.L. supervised the computational study. M.S.K. performed all the experiments, characterizations, and analyses. M.S.K and L.A.A. wrote the manuscript. All the authors discussed the manuscript and provided comments. **Competing interests:** The authors declare that they have no competing interests. **Data and materials availability:** All data needed to evaluate the conclusions in the paper are present in the paper and/or the Supplementary Materials. Additional data related to this paper may be requested from the authors.

Submitted 3 April 2019
Accepted 16 September 2019
Published 25 October 2019
10.1126/sciadv.aax5587

**Citation:** M. S. Kim, Deepika, S. H. Lee, M.-S. Kim, J.-H. Ryu, K.-R. Lee, L. A. Archer, W. I. Cho, Enabling reversible redox reactions in electrochemical cells using protected LiAl intermetallics as lithium metal anodes. *Sci. Adv.* **5**, eaax5587 (2019).

Downloaded from http://advances.sciencemag.org/ on October 31, 2019

Science Advances

# Enabling reversible redox reactions in electrochemical cells using protected LiAl intermetallics as lithium metal anodes

Mun Sek Kim, Deepika, Seung Hun Lee, Min-Seop Kim, Ji-Hyun Ryu, Kwang-Ryeol Lee, Lynden A. Archer and Won Il Cho

*Sci Adv* **5** (10), eaax5587.
DOI: 10.1126/sciadv.aax5587

**ARTICLE TOOLS** http://advances.sciencemag.org/content/5/10/eaax5587

**SUPPLEMENTARY MATERIALS** http://advances.sciencemag.org/content/suppl/2019/10/21/5.10.eaax5587.DC1

**REFERENCES** This article cites 49 articles, 7 of which you can access for free
http://advances.sciencemag.org/content/5/10/eaax5587#BIBL

**PERMISSIONS** http://www.sciencemag.org/help/reprints-and-permissions

Use of this article is subject to the Terms of Service

*Science Advances* (ISSN 2375-2548) is published by the American Association for the Advancement of Science, 1200 New York Avenue NW, Washington, DC 20005. 2017 © The Authors, some rights reserved; exclusive licensee American Association for the Advancement of Science. No claim to original U.S. Government Works. The title *Science Advances* is a registered trademark of AAAS.

Downloaded from http://advances.sciencemag.org/ on October 31, 2019